AGU ADVANCING EARTH AND SPACE SCIENCES

AGU Advances

RESEARCH ARTICLE
10.1029/2023AV001042

"Seeing" Beneath the Clouds—Machine-Learning-Based Reconstruction of North African Dust Plumes

Franz Kanngießer[1,2] and **Stephanie Fiedler**[1,2,3]

[1]Institute of Geophysics and Meteorology, University of Cologne, Cologne, Germany, [2]Now at GEOMAR Helmholtz Center for Ocean Research Kiel, Kiel, Germany, [3]Now at Christian-Albrechts University of Kiel, Kiel, Germany

Peer Review The peer review history for this article is available as a PDF in the Supporting Information.

Key Points:

- We present the first fast reconstruction of cloud-obscured Saharan dust plumes through novel machine learning applied to satellite images
- The reconstruction algorithm utilizes partial convolutions to restore cloud-induced gaps in gray-scaled Meteosat Second Generation-Spinning Enhanced Visible and Infrared Imager Dust RGB images
- World Meteorological Organization dust forecasts for North Africa mostly agree with the satellite-based reconstruction of the dust plume extent

Supporting Information:

Supporting Information may be found in the online version of this article.

Correspondence to:

F. Kanngießer,
fkanngiesser@geomar.de

Citation:

Kanngießer, F., & Fiedler, S. (2024). "Seeing" beneath the clouds—Machine-learning-based reconstruction of North African dust plumes. *AGU Advances*, *5*, e2023AV001042. https://doi.org/10.1029/2023AV001042

Received 15 SEP 2023
Accepted 3 JAN 2024

Author Contributions:

Conceptualization: Franz Kanngießer, Stephanie Fiedler
Data curation: Franz Kanngießer
Investigation: Franz Kanngießer, Stephanie Fiedler
Methodology: Franz Kanngießer
Project administration: Stephanie Fiedler
Resources: Stephanie Fiedler
Software: Franz Kanngießer

Abstract Mineral dust is one of the most abundant atmospheric aerosol species and has various far-reaching effects on the climate system and adverse impacts on air quality. Satellite observations can provide spatio-temporal information on dust emission and transport pathways. However, satellite observations of dust plumes are frequently obscured by clouds. We use a method based on established, machine-learning-based image in-painting techniques to restore the spatial extent of dust plumes for the first time. We train an artificial neural net (ANN) on modern reanalysis data paired with satellite-derived cloud masks. The trained ANN is applied to cloud-masked, gray-scaled images, which were derived from false color images indicating elevated dust plumes in bright magenta. The images were obtained from the Spinning Enhanced Visible and Infrared Imager instrument onboard the Meteosat Second Generation satellite. We find up to 15% of summertime observations in West Africa and 10% of summertime observations in Nubia by satellite images miss dust plumes due to cloud cover. We use the new dust-plume data to demonstrate a novel approach for validating spatial patterns of the operational forecasts provided by the World Meteorological Organization Dust Regional Center in Barcelona. The comparison elucidates often similar dust plume patterns in the forecasts and the satellite-based reconstruction, but once trained, the reconstruction is computationally inexpensive. Our proposed reconstruction provides a new opportunity for validating dust aerosol transport in numerical weather models and Earth system models. It can be adapted to other aerosol species and trace gases.

Plain Language Summary Most dust and sand particles in the atmosphere originate from North Africa. Since ground-based observations of dust plumes in North Africa are sparse, investigations often rely on satellite observations. Dust plumes are frequently obscured by clouds, making it difficult to study the full extent. We use machine-learning methods to restore information about the extent of dust plumes beneath clouds in 2021 and 2022 at 9, 12, and 15 UTC. We use the reconstructed dust patterns to demonstrate a new way to validate the dust forecast ensemble provided by the World Meteorological Organization Dust Regional Center in Barcelona, Spain. Our proposed method is computationally inexpensive and provides new opportunities for assessing the quality of dust transport simulations. The method can be transferred to reconstruct other aerosol and trace gas plumes.

1. Introduction

Mineral dust constitutes one of the major aerosol types in the atmosphere by mass fraction (Pósfai & Buseck, 2010). It has profound direct and indirect effects in the Earth system, for example, by directly affecting atmospheric radiative transfer, by acting as cloud condensation and ice nuclei, and by providing nutrients to terrestrial and marine ecosystems, including the fertilization of the Amazon rainforest by North African dust (e.g., Bristow et al., 2010; Buseck & Pósfai, 1999; Goudie, 2009; Griffin & Kellogg, 2004; Hoose et al., 2010; Kok et al., 2023; Mahowald et al., 2017; Pósfai & Buseck, 2010; P. Seifert et al., 2010; Swap et al., 1992; Talbot et al., 1986). Furthermore, North African dust can be linked to Hurricane activity in the North Atlantic (Evan et al., 2006; Strong et al., 2018). Mineral dust also provides surfaces for chemical reactions and can, thus, act as a sink for certain chemical compounds (Buseck & Pósfai, 1999; Pósfai & Buseck, 2010). In addition to these effects, dust storms have multi-faceted impacts, including disruption of public services, public events, economic activity, and air traffic, as well as reducing photovoltaic energy production, adversely impacting public health, and diminishing agricultural yields (Al-Hemoud et al., 2017; Goudie, 2014; N. Middleton, 2017; Monteiro et al., 2022; Stefanski & Sivakumar, 2009). In addition to reduced air quality by particulate matter, adverse public health impacts also stem from the co-emission of microorganisms, bacteria, fungi, and viruses with dust particles (Griffin, 2007). While Europe itself lacks large source regions of mineral dust, dust transported to Europe is

Supervision: Stephanie Fiedler
Validation: Franz Kanngießer
Visualization: Franz Kanngießer
Writing – original draft: Franz Kanngießer
Writing – review & editing: Franz Kanngießer, Stephanie Fiedler

specifically linked to both adverse impacts on human health, and disruption of transport and public services, but also linked to an enhanced melting of Alpine glaciers when the dust is deposited (Di Mauro et al., 2019; Gabbi et al., 2015; Karanasiou et al., 2012; Oerlemans et al., 2009; Monteiro et al., 2022; Q. Wang et al., 2020).

North Africa is by far the largest source region of mineral dust (Huneeus et al., 2011; Kok et al., 2021, 2023; Tanaka & Chiba, 2006). Due to the sparse ground-based observations in Northern Africa, studying emissions of Saharan dust strongly relies on satellite observations. Dust emission and transport processes are frequently linked with the presence of clouds (e.g., Allen et al., 2013; Ben-Ami et al., 2009; Bou Karam et al., 2010; Bou Karam et al., 2014; Fromm et al., 2016; Heinold et al., 2013; Knippertz & Todd, 2012; Roberts & Knippertz, 2014). Consequently, the full spatial extent of dust plumes as observed by satellite-borne instruments is often obscured by clouds. In this study, we propose to resolve the shortcoming with a novel machine-learning-based reconstruction of North African dust plumes, which employs image in-painting techniques.

Geostationary satellites can provide observations with high temporal resolution. One sensor facilitating this is the Spinning Enhanced Visible and Infrared Imager (SEVIRI), a passive radiometer and the primary instrument onboard the Meteosat Second Generation (MSG) satellites (Schmetz et al., 2002). SEVIRI provides measurements of radiance from 12 different spectral channels and one broadband channel every 15 min. The spectral channels are centered around wavelengths between $\lambda = 0.635$ μm and $\lambda = 13.40$ μm. By combining the information from different instrument channels, false-color RGB images are created. In RGB color spaces, each color can be decomposed into red (R), green (G), and blue (B) components. On these RGB images various atmospheric features, such as different cloud types, air masses, trace gases like SO_2, volcanic ash, and mineral dust can be identified. The RGB product, on which dust features are shown in bright magenta, the Dust RGB, assigns (differences of) brightness temperatures from three infrared bands, specifically $\lambda = 8.7$ μm, 10.8 μm, and $\lambda = 12.0$ μm, to the images' red, green, and blue channels (Banks et al., 2019; Lensky & Rosenfeld, 2008; Schepanski et al., 2007). This product has been used for studies of dust emission frequencies and transport pathways (e.g., Allen et al., 2013; Ashpole & Washington, 2012; Bou Karam et al., 2010, 2014; Dhital et al., 2020; Schepanski et al., 2007, 2012; Solomos et al., 2017; Trzeciak et al., 2017; H. Yu et al., 2021) with the caveat that dust beneath clouds is not visible.

No attempt to resolve the cloud-masking of dust plumes in satellite images has been made to date, but approaches for other cloud-obscured features have been successfully tested. These features were often stationary and often subject to only small temporal changes, such as land cover information (Chauhan et al., 2021; Chen et al., 2020; Czerkawski et al., 2022; Enomoto et al., 2017; L. Liu & Hu, 2021; Li et al., 2020; Pan, 2020; Sarukkai et al., 2020; Singh & Komodakis, 2018; M. Zhao et al., 2021; Zi et al., 2022). Further examples are for land-surface temperature (Sarafanov et al., 2020; Weiss et al., 2014; W. Zhao & Duan, 2020), evapotranspiration (Cui et al., 2020), sea-surface temperature (Dong et al., 2019), and chlorophyll a (Stock et al., 2020).

A substantial amount of dust emissions and consequently transport might be obscured by clouds. Convection-permitting simulations over West Africa indicate a diurnal cycle of dust emission coinciding with cloud cover in summertime West Africa. Between ∼6% (19:00 local time) and up to 55% (10:00 local time) of dust emissions in West Africa occur during clear sky conditions in the simulation (Heinold et al., 2013). Unlike cloud-obscured features like land cover and chlorophyll a, dust storms as well as clouds co-develop in time and space. Dust emission in Northern Africa is frequently linked to outflows from mesoscale convective systems during summer (Allen & Washington, 2014; Allen et al., 2013; Bou Karam et al., 2014; Heinold et al., 2013; Roberts & Knippertz, 2014). A significant amount of North African dust transported over the North Atlantic is above and within the marine boundary layer and interacts with stratiform clouds (Ben-Ami et al., 2009). Baroclinic storms are another mechanisms for long-distance dust transport, which is associated with clouds (Fiedler et al., 2014; Fromm et al., 2016; Schepanski & Knippertz, 2011).

Machine learning methods have been increasingly used for automatic image in-painting, that is, often the repair of damaged or deteriorated photos. In-painting algorithms can be roughly classified into three main types: sequential-based algorithms, convolutional neural net-based algorithms, and generative adversarial networks (GANs)-based approaches. Convolutional neural networks (CNNs) typically capture the global structure better than sequential-based algorithms (Elharrouss et al., 2020). CNNs have been employed for cloud removal, for example, by Chen et al. (2020). Another type of artificial neural networks (ANNs) commonly employed in in-painting and subsequently cloud-removal tasks are GANs (Chauhan et al., 2021; Elharrouss et al., 2020; Enomoto et al., 2017; Jiao et al., 2019; L. Liu & Hu, 2021; Li et al., 2020; Pajot et al., 2019; Stock et al., 2020; J. Yu

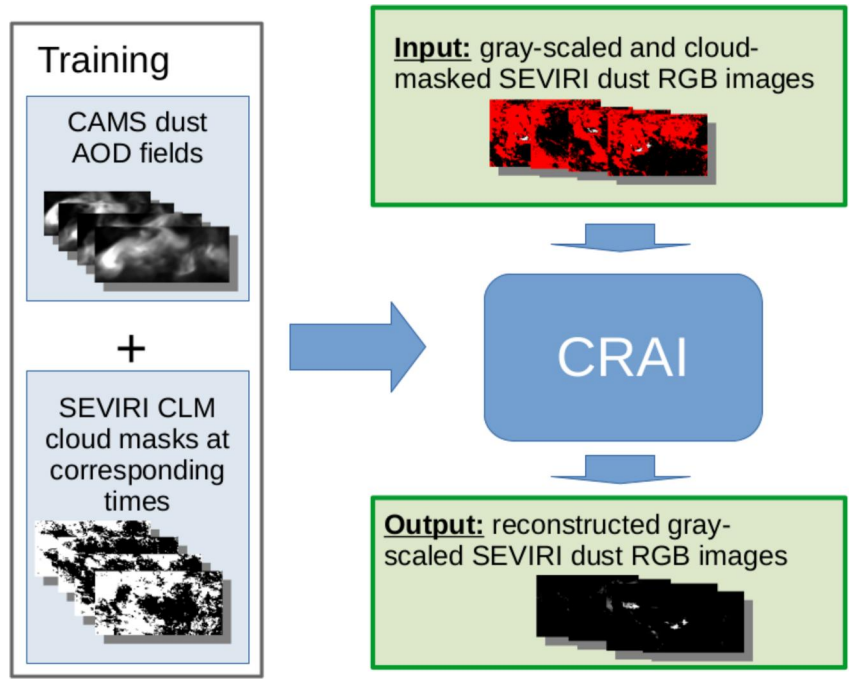

Figure 1. Schematic illustration of this study's set-up. This study relies on the publicly available climatereconstructionAI (CRAI) code (blue box). To train the CRAI we use a combination of dust aerosol optical depth fields provided by Copernicus Atmosphere Monitoring Service and the Meteosat Second Generation-Spinning Enhanced Visible and Infrared Imager (SEVIRI) cloud mask product CLM provided by EUMETSAT (gray-framed box). Once trained, we provide gray-scaled images, we derived from the SEVIRI Dust RGB product, combined with the corresponding cloud mask as input (upper green box). The CRAI provides reconstructed gray-scaled images, in which cloud-masked pixels have been in-painted as output (lower green box).

et al., 2018; Zi et al., 2022). Compared to CNNs, GANs typically require a smaller training data set for in-painting or reconstruction tasks, including in-painting of remote sensing data, and are usually capable of reconstructing large-scale features. Reconstructions by GANs appear realistic, but do not necessarily completely match the ground truth (Dong et al., 2019; Elharrouss et al., 2020; Kadow et al., 2020). Similar to the climate data reconstruction by Kadow et al. (2020) we ultimately attempt a classification, for which it may be disadvantageous if the reconstructions do not necessarily match a ground truth. To avoid such disadvantages, we refrained from using algorithms based on GANs and chose an established CNN-based method.

G. Liu et al. (2018) proposed an algorithm based on partial convolutions, which successfully repaired irregular holes in images. Owning to the similarity to convolutional networks for image segmentation, referred to as UNets (Ronneberger et al., 2015), the algorithm possesses a UNet-like architecture (G. Liu et al., 2018). Furthermore, the algorithm was shown to robustly perform regardless of hole size, location, and distance to the image border and outperformed several other algorithms of all three types. Subsequently, the algorithm was adapted to geophysical data by Kadow et al. (2020). This adapted algorithm, climatereconstructionAI (CRAI, Inoue et al., 2022), was successfully used to restore historical temperature anomalies (Kadow et al., 2020). Owning to the robust performance of the original image in-painting algorithm and the successful adaptation to geophysical data, we use the CRAI code as the basis of our work.

With the aim of restoring the spatial extent of (partially) cloud-obscured dust plumes in North Africa, we employ an ANN, which is described in Section 2.2.1. As illustrated in Figure 1, we train the CRAI algorithm (blue box) on reanalysis data of the dust aerosol optical depth (AOD) (τ_{dust}), which we overlaid with satellite-based cloud masks. This reanalysis data was provided by the Copernicus Atmosphere Monitoring Service (CAMS) (Inness et al., 2019b), indicated by the gray-framed box. The cloud masks were obtained from the MSG-SEVIRI cloud mask product CLM (EUMETSAT, 2009a). The data sets will be described in more detail in Sections 2.1.1 and 2.1.2. To test the trained ANN's performance, we reconstruct reanalysis fields of τ_{dust}, to which we applied the temporally corresponding cloud masks (not shown). The trained ANN is then used to reconstruct the below-cloud

extent of dust plumes by applying it to gray-scaled and cloud-masked images based on the MSG-SEVIRI Dust RGB product (EUMETSAT, 2009b, indicated by the green boxes in Figure 1). The gray-scaling is further described in Section 2.2.2.

This study's aim is to increase the information on the spatial extent of dust plumes over a large area in North Africa, thus, capturing dust plumes across scales including synoptic to meso-scale events. One long-term goal is to provide increased means to both constrain and validate dust plume representations from numerical models, whether they are climate models or forecast models, which currently show large uncertainties (e.g., Evan et al., 2014; Terradellas et al., 2022; A. Zhao et al., 2022).

2. Methods and Data

2.1. Data Sets

2.1.1. Satellite Data Sets

We obtain observational information about the spatial extent of dust plumes from EUMETSAT's MSG-SEVIRI Dust RGB product (EUMETSAT, 2009b). The Dust RGB images were provided by EUMETSAT, reaching back in time to 1 September 2020. They are operationally created by assigning a different combination of brightness temperature observations, T_B, from different SEVIRI infra-red channels to each of the RGB channels, as follows (Lensky & Rosenfeld, 2008):

$$R = \frac{T_{\mathrm{B},12.0\mu\mathrm{m}} - T_{\mathrm{B},10.8\mu\mathrm{m}} + 4\,K}{6\,K} \tag{1}$$

$$G = \left(\frac{T_{\mathrm{B},10.8\mu\mathrm{m}} - T_{\mathrm{B},8.7\mu\mathrm{m}}}{15\,K}\right)^{1/2.5} \tag{2}$$

$$B = \frac{T_{\mathrm{B},10.8\mu\mathrm{m}} - 261\,K}{28\,K} \tag{3}$$

Here the wavelength in the subscripts denotes the wavelength around which the respective channel is centered, with the full spectral width depending on the channel (Schmetz et al., 2002). As a result and as already mentioned, the Dust RGB product features dust plumes in bright shades of magenta. Quartz-mineral-containing sand surfaces are seen in light-blue shades. Depending on the cloud type, clouds may feature in Dust RGB images in brownish shades, black, and/or dark green (Banks et al., 2019; Lensky & Rosenfeld, 2008).

We select data over North Africa, specifically, the region between the longitudes of 20°W and 52°E and the latitudes of 4°N and 40°N. The region is selected such that we obtain a quadratic image that is required for the ANN-based algorithm (see Section 2.2.1). The size of each image was reduced to 128 pixels by 128 pixels to increase the computational throughput. The reduced resolution images were provided by EUMETSAT via its application programming interface, which is compliant with the OpenGIS® Web Map Server Implementation (Version 1.3.0, de la Beaujardiere, 2006), a standard defined by the Open Geospatial Consortium. This reduction in resolution results in each pixel having a dimension of 0.28125° in North-South-direction and 0.5625° in East-West-direction. Thus, each pixel spans roughly 30 km in the North-South direction and 50–60 km in the East-West direction. A pixel's arc length in the East-West direction decreases with increasing distance to the Equator.

Both the training process and the actual dust plume reconstruction rely on the operational cloud mask product, called CLM, and provided by EUMETSAT (EUMETSAT, 2009a). The CLM product classifies pixels as either cloudy or clear. Clear sky pixels are further subdivided according to the surface, that is, land or water surface. This classification is performed based on multispectral threshold techniques (Lutz, 1999; Schmetz et al., 2002). The CLM data used here covers the same region of interest with the same horizontal resolution as the Dust RGB images.

In addition to geostationary satellite data from MSG SEVIRI, we also use satellite data from the Moderate Resolution Imaging Spectroradiometer (MODIS) onboard the satellites Aqua and Terra for a comparison of our results. The satellites Terra and Aqua are orbiting the Earth in a sun-synchronous orbit overpassing the equator in the morning and afternoon respectively (see e.g., King et al., 2013). Here, we use MODIS Level 3 data (Collection

Table 1
Overview of Output From Numerical Forecast Models Provided by the World Meteorological Organization Barcelona Dust Regional Center and the Partners of the Sand and Dust Storm Warning Advisory and Assessment System (SDS-WAS) for Northern Africa, the Middle East and Europe

Model	Domain	Horizontal resolution	Availability 2021 (days)	Availability 2022 (days)	Reference
ALADIN	Regional	25 km × 25 km	301	210	Termonia et al. (2018), Mokhtari et al. (2012)
BSC-DREAM8b	Regional	$\frac{1}{3}^\circ \times \frac{1}{3}^\circ$	176	120	Nickovic et al. (2001), Pérez et al. (2006), Basart et al. (2012)
CAMS-IFS	Global	~9 km[a]	324	353	Rémy et al. (2019)
DREAM8-CAMS	Regional	$\frac{1}{3}^\circ \times \frac{1}{3}^\circ$	328	360	Pejanovic et al. (2010), Nickovic et al. (2016)
EMA-RegCM4	Regional	45 km × 45 km	299	171	Zakey et al. (2006)
ICON-ART	Regional	20 km × 20 km	304	340	Rieger et al. (2015)
LOTOS-EUROS	Regional	0.5° × 0.25°	316	353	Manders et al. (2017)
MOCAGE	Global	1° × 1°	–[b]	226	El Amraoui et al. (2022)
MONARCH	Regional	$\frac{1}{3}^\circ \times \frac{1}{3}^\circ$	343	345	Pérez et al. (2011), Klose et al. (2021)
NASA-GEOS	Global	0.25° × 0.3125°	304	348	Colarco et al. (2010)
NCEP-GEFS	Global	1° × 1°	324	343	Lu et al. (2016)
NOA	Regional	0.19° × 0.22°	111	235	Flaounas et al. (2017)
SILAM	Global	0.5° × 0.5°	222	339	Sofiev et al. (2015)
WRF-NEMO	Regional	18 km × 18 km	82	251	Kontos et al. (2021)
ZAMG-WRF-CHEM	Regional	0.2° × 0.2°	–[b]	198	LeGrand et al. (2019)
MULTI-MODEL (median forecast)	–	0.5° × 0.5°	360	365	Basart et al. (2019), Terradellas et al. (2022)

Note. Model names are as indicated by WMO Barcelona Dust Regional Center. MULTI-MODEL denotes the median forecast as provided by the WMO Barcelona Dust Regional Center. Note that after 29 September 2022, no further operational forecasts were provided by the BSC-DREAM8b model. [a]CAMS-IFS uses a octahedral reduced Gaussian grid (O1280) with a horizontal distance of 8–10 km between grid points (Malardel et al., 2016). [b]Forecasts are only available in 2022.

6.1) (MODIS Atmosphere Science Team, 2017a, 2017b). The data was retrieved using the Deep Blue algorithm, which provides AOD (τ) and Ångström exponent (α) data over land surfaces (Hsu et al., 2013; Sayer et al., 2013).

2.1.2. Dust Forecasts and Reanalysis

In addition to satellite data, our study also uses dust forecast and reanalysis data. Reanalysis data provides a consistent and global overview of τ_{dust}. We use the reanalysis of τ_{dust} from CAMS (Inness et al., 2019a, 2019b) for training the ANN (Section 2.2.1). CAMS dust reanalysis data is provided in three-hourly intervals at the main and intermediate synoptic times, that is, at 00:00 UTC, 03:00 UTC, and so forth. For additional analysis, we also use the second Modern-Era Retrospective analysis for Research and Application (MERRA-2) from NASA (Gelaro et al., 2017; Randles et al., 2016, 2017). MERRA-2 provides hourly data.

We further use the dust forecast data provided by the World Meteorological Organization (WMO) Barcelona Dust Regional Center and the partners of the Sand and Dust Storm Warning Advisory and Assessment System (SDS-WAS) for Northern Africa, the Middle East and Europe. These dust forecasts cover a geographical area of interest, which is bound by the longitudes of 25°W and 60°E and the latitudes of 0°N and 65°N (Terradellas et al., 2022). The WMO Barcelona Dust Regional Center additionally provides a multi-model median of the available forecast data, which is obtained by regridding all other models to a shared grid with 0.5° × 0.5° horizontal resolution using bilinear interpolation (Basart et al., 2022; Terradellas et al., 2022). Table 1 lists the models, their horizontal resolution, and data availability in 2021 and 2022. Of the models listed in Table 1 only CAMS-IFS, DREAM8-CAMS, NASA-GEOS, and MOCAGE employ data assimilation of dust aerosol. MODIS observations form the backbone of the data assimilation. Thus, the numerical dust forecasts can be considered independent of SEVIRI observations. Analogously to the processing of the reanalysis data, the WMO's forecast data was selected for our region of interest and remapped bilinearly to the Dust RGB images' horizontal resolution.

Both reanalysis data and numerical dust forecasts were remapped to the Dust RGB images' resolution of 128 pixels by 128 pixels with bilinear interpolation using CDO, version 2.0.4 (Schulzweida, 2021). The two-dimensional fields at a given time will be referred to as images.

2.2. Dust Plume Reconstruction

2.2.1. ANN and Training Description

We stated in Section 1, we used the publicly available CRAI algorithm (Inoue et al., 2022; Kadow et al., 2020), which is a UNet-like algorithm based on partial convolutions. The original in-painting algorithm, on which the CRAI algorithm is based, was applied to restore irregular holes in photos. To do so, G. Liu et al. (2018) chose a network architecture based on the prior work by Iizuka et al. (2017) and replaced all convolutional layers with partial convolutional layers. The partial convolutional layers were combined mask updates, which provide input for the next partial convolutional layer. In the course of adapting the algorithm to geophysical data, Kadow et al. (2020) reduced the number of partial convolutional layers from seven to three and modified the algorithm further, so it only outputs data on a single channel. The ANN was trained on τ_{dust} data provided by CAMS, introduced in Section 2.1.2. The cloud masks were derived from the temporally corresponding MSG-SEVIRI product. To be more specific, we applied the available CLM clouds masks for a given time to the corresponding reanalysis field of τ_{dust} for this same time step. This is indicated in the gray box in Figure 1. We chose to use observed cloud patterns and refrained from using synthetic clouds for training purposes, since the latter may introduce unrealistic patterns during the training process (Enomoto et al., 2017). In addition, both the dust outbreak and the cloud cover are subject to the same atmospheric state, especially the pressure and wind fields. Combining cloud-free satellite images with a set of different cloud masks, thus, would pose the risk of training the ANN on non-physical combinations of cloud and dust patterns. We eliminate such risks by using masks of satellite-observed clouds.

The training was performed on the German Climate Computing Center's (Deutsches Klimarechenzentrum, DKRZ) cluster Levante. Specifically, we used the cluster's GPU partition, on which each node consists of two CPUs equipped with AMD 7713 processors and four Nvidia A100 GPUs. The training required ∼13 hr of wall-time.

For initial tests, the trained neural network was applied to the CAMS reanalysis fields of τ_{dust} from 1 January 2022 to 30 June 2022. Data from this period was exclusively used for these initial tests. Analogously to the training data set, the reanalysis was masked with the MSG-SEVIRI cloud mask product. Figure 2 shows two-dimensional histograms of the mean CAMS reanalysis on the x-axis and the mean reconstruction on the y-axis. The different panels represent different sizes of the training data set. The first training data set consists of a total of 16 months, spanning from 1 September 2020 to 31 December 2021 (Figure 2a). For three-hourly time steps as dictated by the reanalysis data with occasionally missing cloud-mask data from SEVIRI, we obtained 3,843 pairs of masks and reanalysis "images." This training data set was augmented by rotating the images by 90°, thus quadrupling the data set size to a total of 15,372 images (Figure 2b). Additional non-augmented training data sets comprised half a year each, and are shown for summer: 1 April 2021 to 30 September 2021 (1,422 images, Figure 2c) and winter: 10 January 2020 and 31 March 2021 (1,449 images, Figure 2d). While previous work on cloud removal has employed augmentation to increase the training data set (e.g., Li et al., 2020), the satellite images covered a smaller area. The simple augmentation technique of rotation of the quadratic images, which cover a considerable spatial extent, by 90° may pose the risk of introducing combinations of spatial cloud and dust patterns, which are unlikely to be representative of true atmospheric motion. This risk is not directly mitigated and, thus, may counteract potential improvements gained from an increased size of the training data set.

As can be inferred from Figure 2 and the values of root mean squared error (RMSE), mean absolute percent error (MAPE), and r, there is generally good agreement between the mean reconstructed τ_{dust} and the mean τ_{dust} from reanalysis.

While the ANN trained for summer marginally outperforms the non-augmented training data set of 16 months with respect to RMSE, MAPE, and r, we chose the ANN trained on the data set with 16 months of reanalysis and corresponding cloud mask data (Figure 2a) since it covers more than a full year, which captures some seasonal differences in spatial patterns of τ_{dust}.

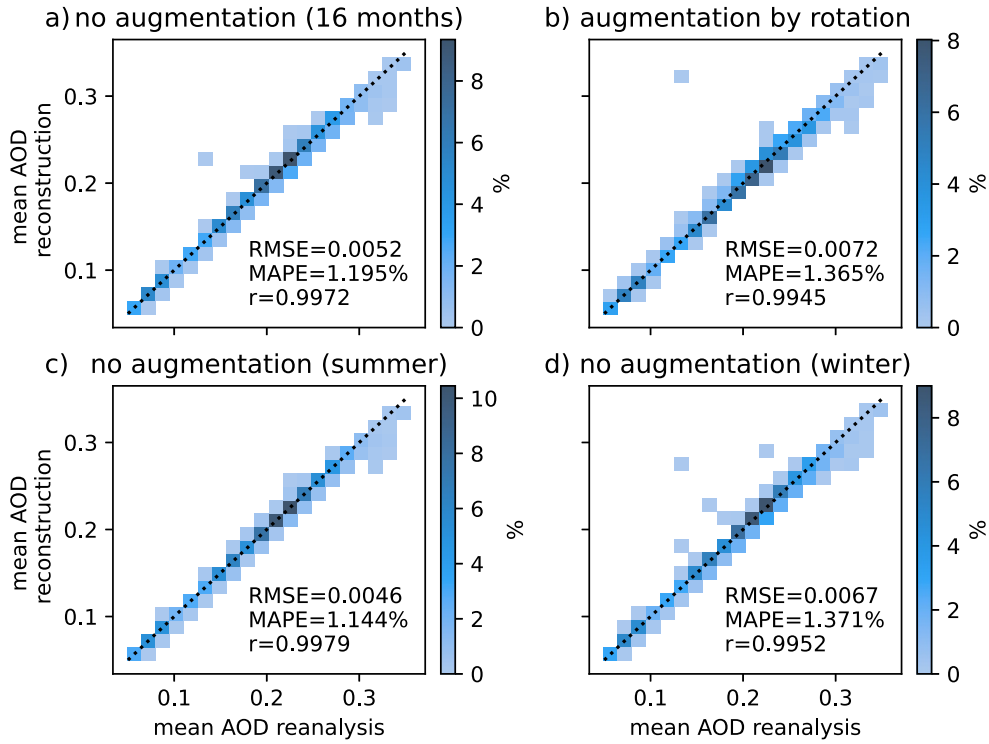

Figure 2. Two-dimensional histograms of the mean non-masked τ_{dust} from Copernicus Atmosphere Monitoring Service reanalysis and the mean reconstructed τ_{dust}. The shading represents the density of the data points in the respective size bin with white indicating no available data. For each panel, the root mean squared error and the mean absolute percent error of the reconstruction with respect to the reanalysis are given. Furthermore, the Pearson correlation coefficient r between reconstructed and original, that is, non-masked, reanalysis is shown.

Since domain averages of τ_{dust} may obscure differences in the information on the spatial patterns in the original and reconstructed reanalysis fields of τ_{dust}, we calculated the structural similarity index measure (SSIM) between the original and the reconstructed reanalysis fields. The SSIM quantifies the perceived differences in structural information between two images (Z. Wang et al., 2004). It is a composite measure of means (or luminance), standard deviations (or contrast), and correlation coefficient (or structure) (Brunet et al., 2012; Palubinskas, 2014; Z. Wang et al., 2004). The SSIM takes values between −1 and 1. The higher the agreement of two images, the closer the SSIM is to 1. Several studies on image in-painting and cloud removal applications have used SSIM as an evaluation criterion (e.g., Chauhan et al., 2021; Czerkawski et al., 2022; Qin et al., 2021; Li et al., 2020; G. Liu et al., 2018; Zi et al., 2022). We calculate SSIM using the implementation in the software package scikit-image (van der Walt et al., 2014).

To further validate the reconstruction, we also calculated the anomaly correlation coefficient (ACC) as defined by Jolliffe and Stephenson (2011) between the original and the reconstructed reanalysis. The ACC, a tool used for validating numerical forecasts, calculates the Pearson's correlation coefficient between the anomalies of a forecast and an analysis of a climatological value. Here, we considered the reconstructed reanalysis field as our forecast and the original reanalysis as our analysis. For each day and time, we calculated the 15-year mean of τ_{dust} from CAMS reanalysis between 1 January 2005 and 31 December 2019. The distribution of the ACC values for the four training data sets is shown in Figure 3 in the form of a violin plot (Hintze & Nelson, 1998). While for individual pairs the ACC can take values as low as ∼0.1, both the median and the mean value of the ACC, indicate high agreement between the reconstructed and the original reanalysis. The distribution of values of SSIM also indicates a high agreement in terms of structural information between the reconstructed and the original reanalysis fields. The mean and median values are show above the corresponding distribution as med (ACC) (and med $(SSIM)$) and $\overline{ACC}$ (and $\overline{SSIM}$) respectively.

To further assess the quality of the reconstruction examples of the unmasked reanalysis (left column) and the corresponding masked reanalysis (center column), and reconstruction (right column) are shown in Figure 4. The

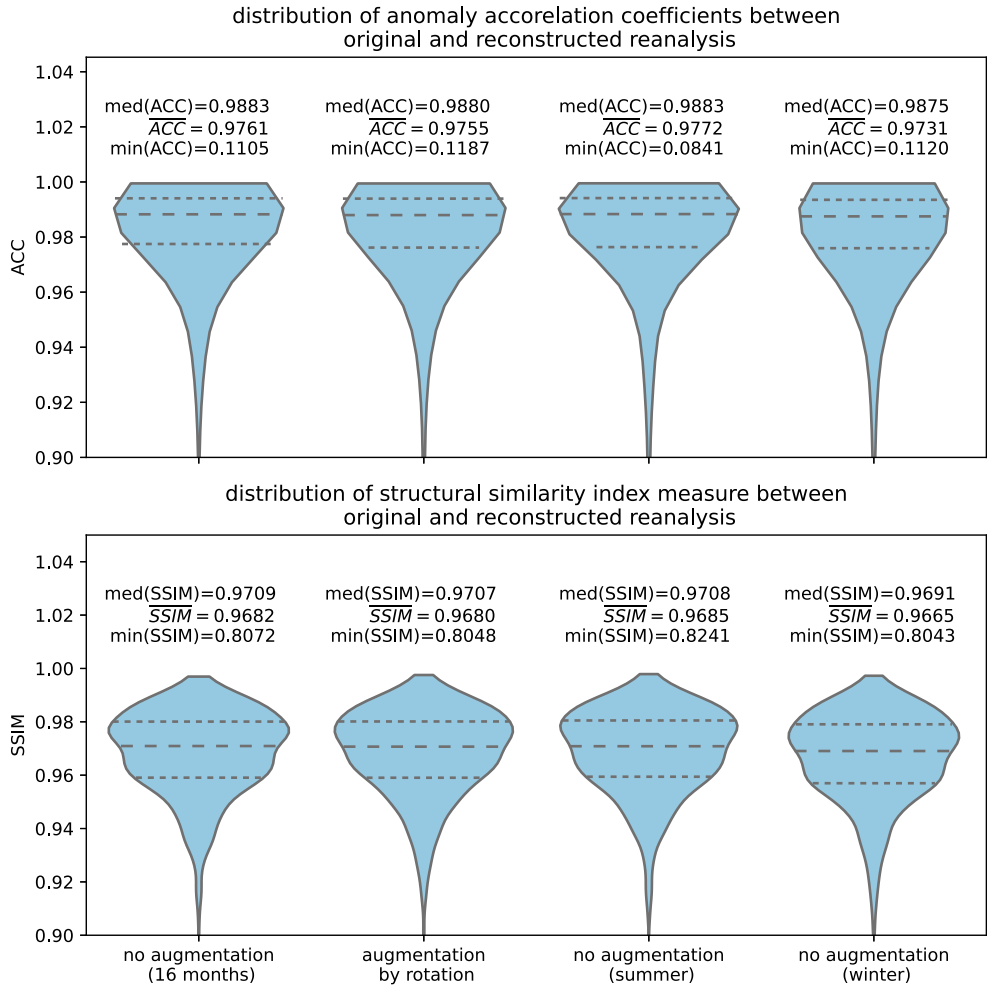

Figure 3. Distribution of anomaly correlation coefficients (top panel) between original and reconstructed dust aerosol optical depth reanalysis. Anomalies were calculated with respect to the 15-year mean for each day and time, as obtained from Copernicus Atmosphere Monitoring Service reanalysis from 2005 to 2019. The bottom panels shows the distribution of the structural similarity index measure between the reconstruction and the corresponding original reanalysis field. Long-dashed lines indicate the median value, whereas, short-dashed lines indicate the first and third quartiles.

rows represent different examples of reconstructions, showcasing the reconstructions for which we have seen the best performance as well as the two reconstructions with the poorest agreement with the original reanalysis. The first row shows the case of 6 January 2022, 6:00 UTC. For this case, the reconstruction and original reanalysis showed the highest agreement, quantified by both the RMSE and the directed Hausdorff distance. The directed Hausdorff distance is a measure of image (dis)similarity. A directed Hausdorff distance of zero indicates perfect agreement. It will be introduced in more detail in Section 3.3. The ACC for this case was 0.9988 and the SSIM was 0.9918. The reconstruction from 3 February 2022 at 9:00 UTC resulted in an overestimated mean of τ_{dust}. This case is represented by the individual point visible in both top row panels of Figure 2, which is farthest from the 1:1 line. That difference between reconstruction and reanalysis results in an RMSE of 4.975, the largest between two individual images. This difference results in an ACC of 0.1370 and a SSIM of 0.9595. Closer inspection in Figure 4 reveals, that the deviation can be attributed to a limited number of pixels north of the Madeira Archipelago filled with high very high values of τ_{dust}. The reconstruction for 16 March 2022, 03:00 UTC, which has the largest value of the directed Hausdorff distance between the reconstruction and the ground truth, an ACC of 0.7118, and a SSIM of 0.9408, is shown the third row of Figure 4. The trained ANN was not able to reconstruct the full spatial pattern of the dust plume, which is the prominent feature of the image's western half. The strong advection of dust over the Iberian Peninsula was not reproduced in the reconstruction. Such infrequent cases of strong dust advection, in which the dust plume is largely obscured by clouds extending to the image boundary

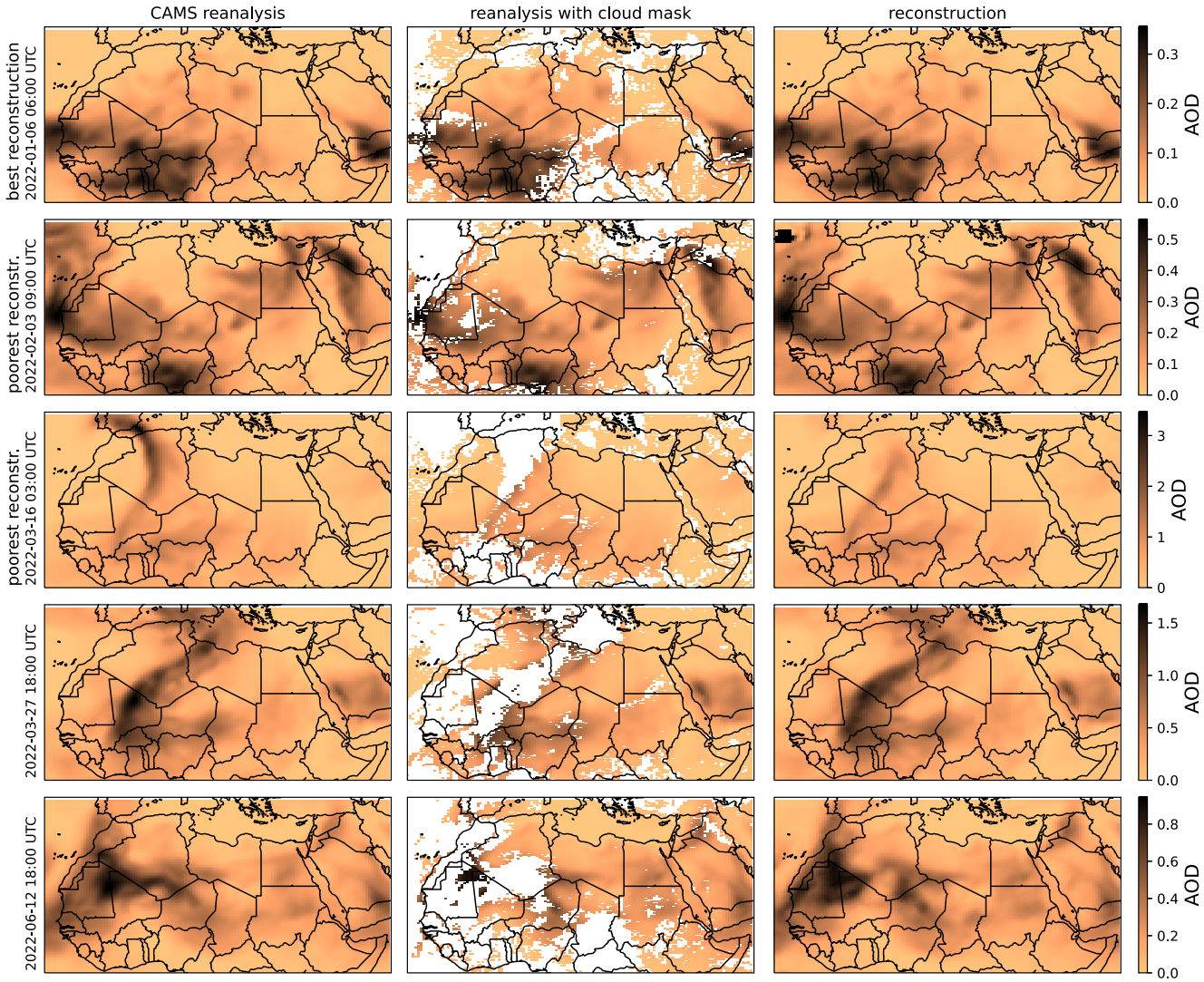

Figure 4. Comparison of Copernicus Atmosphere Monitoring Service (CAMS) reanalysis used as ground truth (left column), cloud-masked CAMS reanalysis, used as input (center column), and reconstruction (right column) for five different cases, represented by the rows. Note, that rows 2 and 3 represent the reconstructions resulting in the largest deviations from the ground truth with respect to root mean squared error (Case 3 February 2022, 09:00 UTC) and directed Hausdorff distance (Case 16 March 2022, 03:00 UTC).

over the ocean, can be considered particularly challenging for reconstruction. However, while the reconstruction did not fully reproduce the spatial pattern of τ_{dust}, the reconstruction added information compared to the cloud-masked input. The fourth row shows a case (27 March 2022, 18 UTC) from a period of high mean values of τ_{dust} in the study area with an ACC of 0.9928 and a SSIM 0.9711. The case from 12 June 2022, 18 UTC, shown in the fifth row, was randomly selected from the month of June 2022. The ACC for this case was 0.9680, while the SSIM was 0.9404.

As demonstrated in Figures 2–4 the trained ANN is capable of successfully reconstructing the cloud-obscured values and patterns of τ_{dust} during the first half of 2022. The reconstruction's purpose is to classify individual pixels as dust-containing or dust-free. Thus, we consider the error stemming from pixels filled with high values of τ_{dust} during the reconstruction, as for the case of 3 February 2022 at 9:00 UTC (see Figure 4) as negligible.

2.2.2. Gray-Scaling of Dust RGB Images

Prior to reconstructing the spatial extent of dust plumes, we isolated the dust in the satellite observations. To do so, the images from MSG-SEVIRI's Dust RGB product were converted to gray-scaled images, where gray

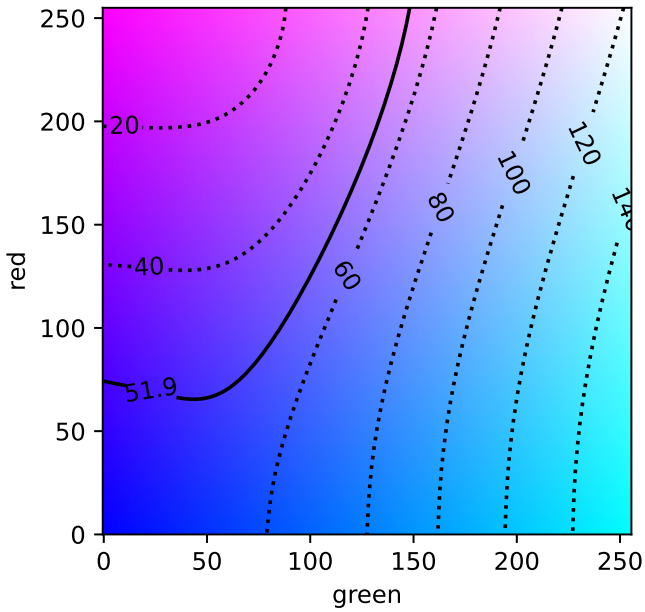

Figure 5. RGB colors as a function of value of the red component (along *y*-axis) and the green component (along *x*-axis) for a fixed value of the blue component of 255. Isolines indicate perceptional color differences ΔE calculated using Equation 4. For most parts of our study, we set $\Delta E_{cut} = 51.9$, indicated by the solid line.

corresponds to pink color shadings assigned to suspended dust in the original Dust RGB product. In other words, we reduced the satellite images, which consisted of the three RGB channels, to a gray-scaled, that is, single channel, image. The gray-scaling was based on perceptional color differences. Gray-scaling is performed to reduce the complexity of the dust identification in satellite images by using only a one-dimensional data in different gray scales. In addition, the CRAI algorithm used in this study, requires one-dimensional or single-channel data. These perceptional color differences were calculated according to definitions by the International Commission on Illumination (Commission Internationale de l'Éclairage, CIE) (Robertson, 1990) in CIE-LAB color space. To do so the RGB colors in the images provided by EUMETSAT need to be converted to CIEXYZ color space and further to CIELAB. The conversion was based on the assumption, that EUMETSAT uses the sRGB color space, which is the standard for digital online images (International Electrotechnical Commission, 1999). The conversion to CIEXYZ was performed analogously to the conversion laid out by Fairman et al. (1997), Brill (1998), but using the conversion matrix values as defined by the sRGB standard (International Electrotechnical Commission, 1999).

Each RGB channel has values between 0 and 255. Thus, white would correspond to (0, 0, 0) and black to (255, 255, 255). In the CIEXYZ color space, the luminance is encoded in Y and the XZ plane includes all possible chromaticities at a value of Y. In the CIELAB color space, L^* denotes the lightness, a^* represents the green-red-oriented axis, and b^* represents the blue-yellow-oriented axis. Negative values of a^* indicate green, whereas, negative values of b^* indicate blue. The positive values represent red and yellow on the respective axis (Schanda, 2007). CIELAB forms a Cartesian and nearly uniform color space, which eases the quantification of perceptional color differences ΔE. ΔE is defined by Robertson (1990)

$$\Delta E = \left[(\Delta L*)^2 + (\Delta a*)^2 + (\Delta b*)^2\right]^{\frac{1}{2}}. \quad (4)$$

ΔL^*, Δa^*, and Δb^* denote the differences between the corresponding values of L^*, a^*, and b^* of the respective colors.

Equation 4 forms the basis of the conversion of Dust RGB images, in which dust plumes are seen as bright magenta (pink), to gray-scale images. In these gray-scale images, magenta ($RGB = (255, 0, 255)$) was assigned to white. Colors exceeding a pre-defined threshold value of the perceptional color difference ΔE compared to magenta were assigned black. Gray values were assigned based on values of ΔE below the threshold. We denote the threshold for identifying dust in the image as ΔE_{cut}.

We identify the value of the threshold based on earlier studies and own sensitivity tests. Banks et al. (2019) investigated the effect of different environmental conditions, such as column water vapor, surface emissivity, skin temperature, and dust layer height on the color in the RGB Dust product using radiative transfer calculations. This investigation focused on the months of June and July in 2011, 2012, and 2013. They identified only a limited number of cases (0.04% of day-time cases and 5.47% of night-time cases), which resulted in RGB colors with values of the blue channel other than 255. Figure 5 shows the colors for a fixed value of the blue component of 255 and variable values of the red (*y*-axis) and the green (*x*-axis) components. The corresponding values of ΔE with respect to magenta with $RGB = (255, 0, 255)$ are shown as isolines. Furthermore, Banks et al. (2019) provided an overview of the mean colors stemming from the combinations of aforementioned conditions. For near-pristine cases, the τ_{dust} was assumed to take values with $\tau_{dust} \leq 0.2$. For unambiguous cases of dust storms, Banks et al. (2019) set $\tau_{dust} \geq 2$. Using Equation 4 the perceptional color difference ΔE between these mean colors reported by Banks et al. (2019) and magenta with $RGB = (255, 0, 255)$ was calculated. For the different mean pristine cases, the perceptional color difference takes values with $19.4 \leq \Delta E \leq 129.4$, whereas, for mean cases with a dust load ΔE takes values in the range of 29.7 and 88.0. However, when additionally taking the skin temperature T_{skin} into account, the resulting ranges are for cool ($T_{skin} < 300$ K), pristine mean cases in

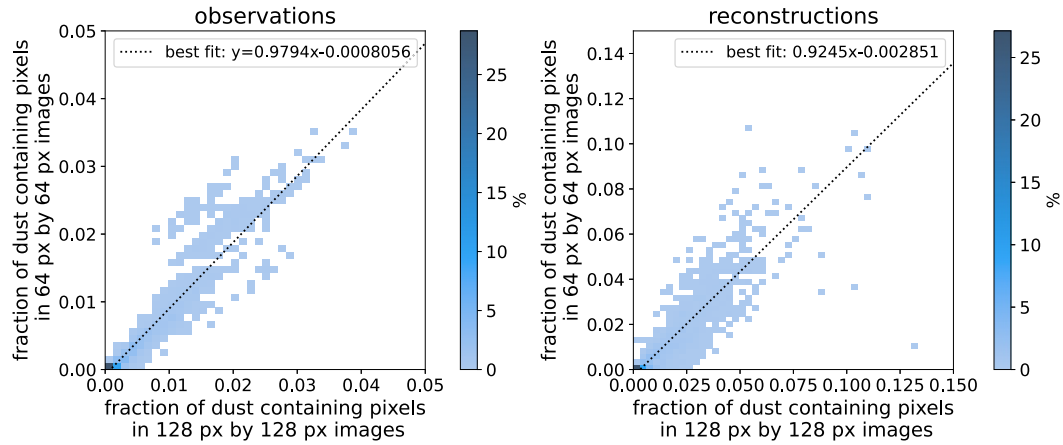

Figure 6. Two-dimensional histograms showing fraction of dust containing pixels in the gray-scaled, cloud-obscured Dust RGB images in coarser and finer resolution (left) and the artificial neural net-based reconstruction (right). Shading is as in Figure 2. The dashed line indicates the best fit, obtained by using linear regression.

$19.4 \leq \Delta E \leq 92.6$, for non-cool, that is, $T_{\text{skin}} > 300$ K, pristine cases $60.2 \leq \Delta E \leq 129.4$. For cool dust cases ΔE is in the range between 29.7 and 72.3 and respectively in the range between 31.0 and 88.0 for non-cool dust. As a consequence, the night-time observations, which are considered to represent the cases of a cool skin temperature are excluded from the reconstruction. Note, that we use the classification of cases as defined by Banks et al. (2019). We set the cut-off threshold in our gray-scaling algorithm to $\Delta E_{\text{cut}} = 51.9$, marked with a solid isoline in Figure 5. With this choice of ΔE_{cut}, pristine cases are not expected to be falsely considered as dust cases, while the true number of dust cases is potentially underestimated. Prior to the process of in-painting (see, Kadow et al., 2020), the gray-scaled images are scaled to values between 0 and 1 as opposed to values between 0 and 255.

2.2.3. Effects of Coarser Spatial Resolutions on Plume Detection

Full-resolution Dust RGB images and cloud masks have a spatial resolution in nadir direction of 0.041° or 4.8 km (EUMETSAT, 2009a, 2009b; Schmetz et al., 2002). The images used in this study possess a coarser resolution of 0.28125° in North-South-direction and 0.5625° in East-West-direction. Due to this coarser resolution compared to the full resolution images, it is expected that resampling of the satellite products, especially the Dust RGB product, results in under-counting the number of dust-containing pixels in addition to under-counting due to the choice of ΔE_{cut} (see above). This is expected to mainly concern dust plumes of small spatial scale in one dimension. To gauge the effect of the resampling, the images were resampled from a 128-pixel by 128-pixel grid to a 64-pixel by 64-pixel grid, that is, each pixel in these coarser resolution images corresponds to 0.5625° in North-South-direction and 1.125° in East-West-direction. Subsequently, we trained another ANN using this coarser resolution. Note, however, that this additionally trained ANN was only used to gauge the impact of the image resolution. We will refer to the images with a size of 128 pixels by 128 pixels as high-resolution images and to the images with a dimension of 64 pixels by 64 pixels as low-resolution images.

We test to what extent the spatial resolution of the satellite data might have an influence on the results. To that end, Figure 6 shows two-dimensional histograms of the fraction of dust-containing pixels in low-resolution images (64 pixels by 64 pixels) and high-resolution images (128 pixels by 128 pixels). Here, observations and the corresponding reconstructions at 9, 12, and 15 UTC were considered. The left panel refers to the direct observations, that is, the gray-scaled, cloud-obscured Dust RGB images and the right panel refers to the ANN-based reconstructions. The dashed line indicates the best fit, which was obtained by linear regression. Regardless of the resolution, the fraction of dust-containing pixels is generally maintained, as can be inferred from the equation for the best fit and the shape of the histograms. This is also reflected by the Pearson's correlation coefficient of $r = 0.94$ in the case of the direct observations and of $r = 0.93$ in the case of the reconstructions. The reconstruction maintains the general pattern well, as illustrated by the nearly unchanged value of r. Note, that the time required for training on the low-resolution images (64 pixels by 64 pixels) required roughly half the time, compared to the training on the high-resolution images (128 pixels by 128 pixels). Taking the high-resolution images as a

reference, the coarser resolution results in a MAPE of the fraction of dust-containing pixels of 46.59% for the observations and 55.04% for the reconstructions. Thus, a finer resolution decreases the under-counting of dusty areas and improves the reconstruction's quality. As a consequence, there are trade-offs between the reconstruction's quality and the reduced risk of under-counting dust-containing pixels on the one hand and the training process' computational demand on the other hand. For the remainder of this study, the higher spatial resolution of 128 pixels by 128 pixels was used to detect more spatial details of dust plumes.

2.2.4. Evaluation Methods

The level of agreement between the dust plume extent from our reconstructions and numerical forecasts was evaluated using three different criteria, which have previously been employed to quantify image similarity. Among these criteria is the SSIM, which has been introduced in Section 2.2.1.

Billet et al. (2008) used the directed Hausdorff distance to assess similarities between two images. As mentioned in Section 2.2.1, the directed Hausdorff distance between two images is the largest distance of a point in the test image to any point in the reference image. Thus, identical images have a directed Hausdorff distance of 0, and with increasing differences between the images, the directed Hausdorff distance increases (Huttenlocher et al., 1993). We calculated the Hausdorff distance of images from our reconstruction and from numerical forecasts of individual models relative to the image from the median across all available numerical forecasts, which we chose as a reference. Note, that the directed Hausdorff distance is asymmetric. In other words, the directed Hausdorff distance from our reconstruction to the median forecast is not necessarily equal to the directed Hausdorff distance from the median forecast to our reconstruction. In this study the directed Hausdorff distance was calculated using the implementation in SciPy (Virtanen et al., 2020), which is based on work by Taha and Hanbury (2015).

Another commonly used performance evaluation metric in image in-painting and cloud removal studies (e.g., Elharrouss et al., 2020; G. Liu et al., 2018; Pan, 2020; Qin et al., 2021; Sarukkai et al., 2020; Zi et al., 2022) is the peak signal-to-noise ratio (PSNR). The PSNR is defined as (Horé & Ziou, 2013)

$$PSNR = 10 \cdot \log_{10} \frac{\max(I_{\text{ref}})^2}{MSE}. \tag{5}$$

Here the mean squared error is denoted as MSE. The MSE between an image I and a reference image I_{ref}, which both consist of $n \cdot m$ pixels is calculated by:

$$MSE = \frac{1}{nm} \sum_{i=1}^{n} \sum_{j=1}^{m} (I_{ij,ref} - I_{ij})^2 \tag{6}$$

For the binary images in our study, $\max(I_{\text{ref}})$ is equal to 1 and Equation 5 can be simplified to $PSNR = 10 \cdot \log_{10} MSE^{-1}$. With increasing similarity between two images $MSE \to 0$, and $PSNR \to \infty$.

3. Results

3.1. Case Studies

We first perform two case studies to test our reconstructions and to gauge their ability to serve as a tool for evaluating numerical forecasts of dust storms. Here we focus on observed dust cases that can be considered as hard tests of our proposed method. The first case concerns a convective dust storm during summer. The numerical models (see Table 1) are not expected to accurately forecast the dust plume, since their horizontal resolution is too coarse to explicitly simulate convection (cf. Weisman et al., 1997). However, this may also present challenges for the training data set, since the dust reanalysis depends on available satellite observations as well as an underlying numerical forecast model. The second case study covers a synoptic-scale dust storm in spring. While the horizontal resolution of the numerical models is not expected to represent a challenge, the satellite image indicates that a large part of the dust storm is entirely obscured by clouds, thus providing little guidance on the spatial distribution of the dust plume in the cloudy sky.

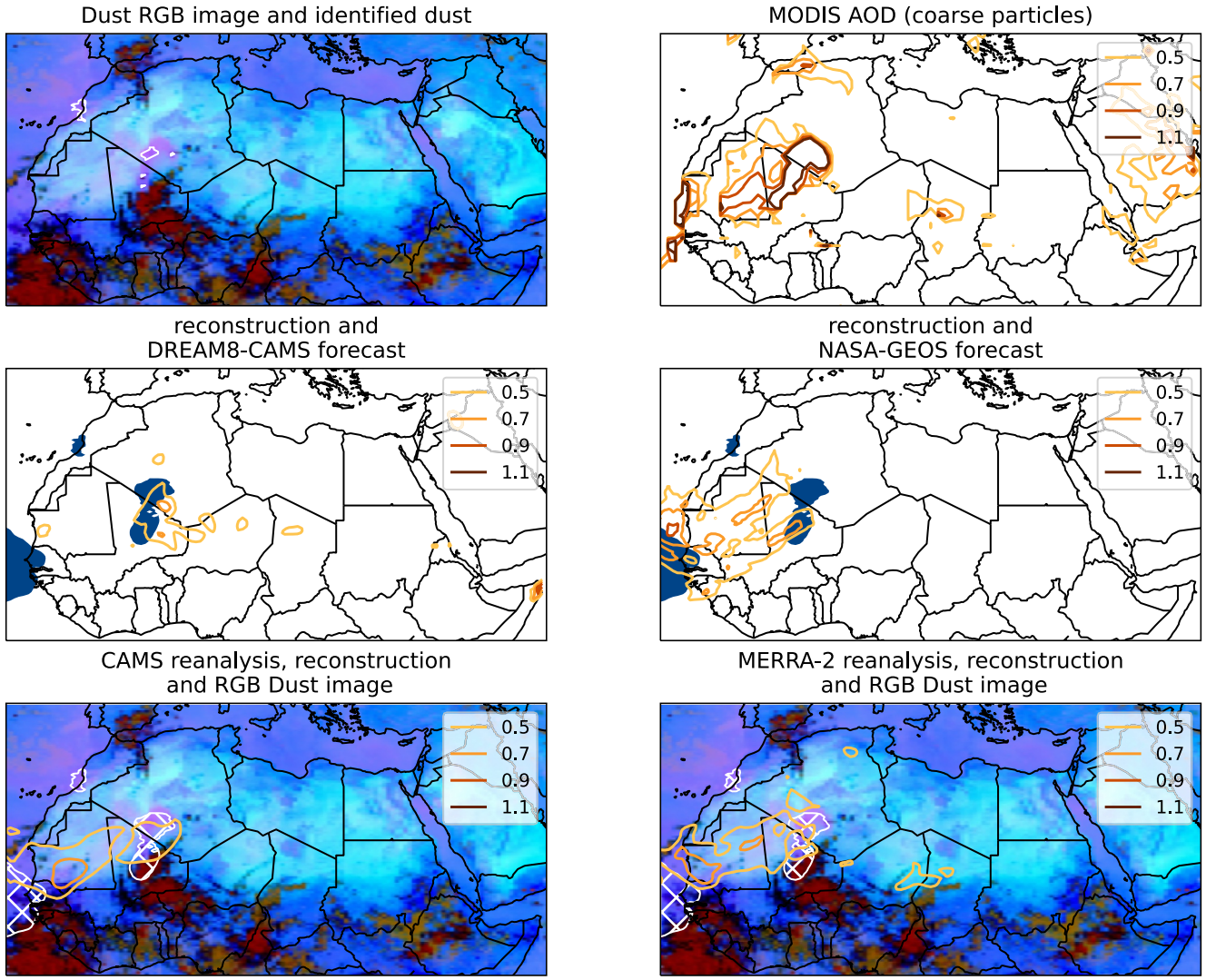

Figure 7. Comparison of Spinning Enhanced Visible and Infrared Imager (SEVIRI) and Moderate Resolution Imaging Spectroradiometer (MODIS) observations with results from numerical dust forecasts, artificial neural net-based reconstructions and reanalysis data for 22 August 2021, 09 UTC. Top right panel show Dust RGB image in 128 pixel by 128 pixel resolution and dust plumes detected by applying gray-scaling are indicated by white contours. The top left panel shows τ from MODIS/Terra observations for coarse particles ($\alpha > 0.75$) with isolines indicating the different values. The middle panels show the reconstructed dust plumes in dark blue and the isolines show the forecasted values of τ_{dust}. The forecast shown in the left panel was obtained from the DREAM8-CAMS model and the forecast in the right panel from the NASA-GEOS model. The bottom panels show SEVIRI Dust RGB images as in the top right panel. White, hatched contours indicate reconstructed dust plumes, whereas, isolines indicate the values of τ_{dust} from Copernicus Atmosphere Monitoring Service (left panel) and MERRA-2 (right panel) reanalysis.

3.1.1. Convective Dust Storm: 22 August 2021, 09 UTC

The Dust RGB image from 22 August 2021 at 09:00 UTC is characterized by a dust plume extending from Northern Mali to Southern Algeria. Visual inspection of the full-resolution Dust RGB images reveals that dust was originally lofted close to a convective cloud system at around 16:00 UTC on 21 August 2021 near the border between Algeria and Niger. Starting from 23:15 UTC the dust plume decoupled from the motion of the convective system and now followed an independent track. With the chosen threshold of the perceptional color difference of $\Delta E_{\text{cut}} = 51.9$ the gray-scaling approach does not identify the entire dust plume, as can be seen in the top left panel. This serves as an example of potential under-counting of dust pixels (see Section 2.2.2). In Figure 7, the top left panel shows the Dust RGB image in 128 pixels by 128-pixel resolution and highlights by white lines the areas in which dust was detected. The top right panel shows τ as derived from observations by the MODIS instrument aboard Terra. Note that this MODIS Level 3 product does not coincide with 09:00 UTC, but represents the closest

overpass of Terra in time. Terra overpasses the Equator at 10:30 local time (cf., King et al., 2013). The panels in the center row show a comparison between the spatial extent of the reconstruction (dark blue shading) and forecasted fields of τ_{dust} from two numerical models (isolines). Since the horizontal resolution of the dust forecast model ensemble (see Table 1) is too coarse to explicitly simulate deep convection on the model grids (Kain et al., 2008), the forecast models are not expected to accurately predict associated dust plumes (Heinold et al., 2013).

The MODIS/Terra observations of τ also indicate the presence of coarse aerosol at and near the Bodélé Depression in Chad. The DREAM8-CAMS model forecasts a small dust plume near the Bodélé Depression. While the Dust RGB image in 128 pixels by 128-pixel resolution does not indicate the presence of dust plumes at the Bodélé Depression, however, the full-resolution Dust RGB images show the presence of a small dust plume in the Bodélé Depression. As discussed in Section 2.2.2, rescaling Dust RGB images to coarser resolutions leads to undercounting dust plumes of small spatial extent. Thus, the resulting RGB color values in each pixel may differ too strongly from magenta, that is, possess large perceptional color differences ΔE. At first, dust emitted by convective systems is completely covered by clouds. Heinold et al. (2013) estimated based on convection-permitting simulations, that up to 90% of afternoon-to-evening dust emissions occur in partly cloudy conditions, and up to 60% of afternoon-to-evening dust emissions occur during strongly cloud-covered conditions, with total cloud cover exceeding 80%. In this case study, dust can first be discerned on the satellite image at 16:00 UTC, making it a prime example of the emission mechanisms discussed by Heinold et al. (2013).

3.1.2. Synoptic-Scale Dust Storm: 15 March 2022, 12 UTC

During mid-March 2022 high loads of Saharan dust were transported to Central Europe via the Iberian Peninsula (cf. A. Seifert et al., 2023). This second case study concerns 12:00 UTC on 15 March 2022 (Figure 8). The region of interest's western part is dominated by a cyclone and its associated cloud patterns over the Iberian Peninsula extending southward across Morocco and Algeria. Dust plumes are visible over large areas of Algeria. Furthermore, magenta colors indicate the presence of dust over Chad, Niger, Burkina Faso, Sudan, and Egypt. The regional plumes along the border between Burkina Faso and Niger, as well as the ones in Egypt are not displayed in the gray-scaled images, with the exception of a small area in Egypt. As stated in Section 2.2.2 the choice of ΔE_{cut} is such that we use the clearly identifiable dust pixels with intense magenta well aware that this approach leads to a conservative estimate of number of dusty pixels. Specifically, the dust plumes over Egypt are organized as thin streaks, which are less prominently visible after resampling the dust RGB images to a grid of 0.28125° by 0.5625°. It is worth pointing out, that the darker magenta of Southern Niger and Northern Nigeria is likely caused by clouds, as indicated by visual inspection of the full-resolution images. Thus, these pixels are correctly identified as dust-free.

The reconstructed dust plume stretching from the Iberian Peninsula toward the Algerian-Malian border is meteorologically plausible. This large dust plume is simulated by the forecasts of both DREAM8-CAMS and BSC-DREAM8b. However, the dust plume's forecasted position over the Mediterranean and the Iberian Peninsula differs from the reconstruction. In the case of the BSC-DREAM8b forecast, the dust plume extends across Mali to the Malian-Guinean border region. Visual inspection of the original resolution images indicates the presence of thin low-level clouds across Mali instead of dust. While the DREAM8-CAMS dust forecast indicates some dust in Sudan, both models fail to accurately forecast the dust plumes in Sudan and Egypt. The dust plumes in Egypt are captured by neither the CAMS reanalysis nor the MERRA-2 reanalysis. Both reanalysis products, however, indicate a strong presence of mineral dust with values of $\tau_{dust} > 1.1$ in Sub-Saharan West Africa. This corresponds to the values observed by MODIS for coarse aerosol particles. The Dust RGB image, including the full-resolution image, does not indicate dust this far south. However, as evident from the simulations by Banks et al. (2019), environmental and surface conditions may mask dust in Dust RGB images. Even though MODIS observations of coarse aerosol are not necessarily solely attributable to mineral dust, mineral dust may still extend further south, than indicated by the Dust RGB image. Since both CAMS and MERRA-2 use MODIS satellite observations to gain information on aerosol properties (Gelaro et al., 2017; Inness et al., 2019b; Randles et al., 2016, 2017; Rémy et al., 2019), observations from additional satellite sensors may increase the agreement between the reanalysis and the reconstructed spatial patterns of mineral dust. Furthermore, this case study illustrates, that synoptic-scale dust storms are still challenges for numerical forecast models, for example, documented earlier for another case advecting dust over the Iberian Peninsula (Huneeus et al., 2016).

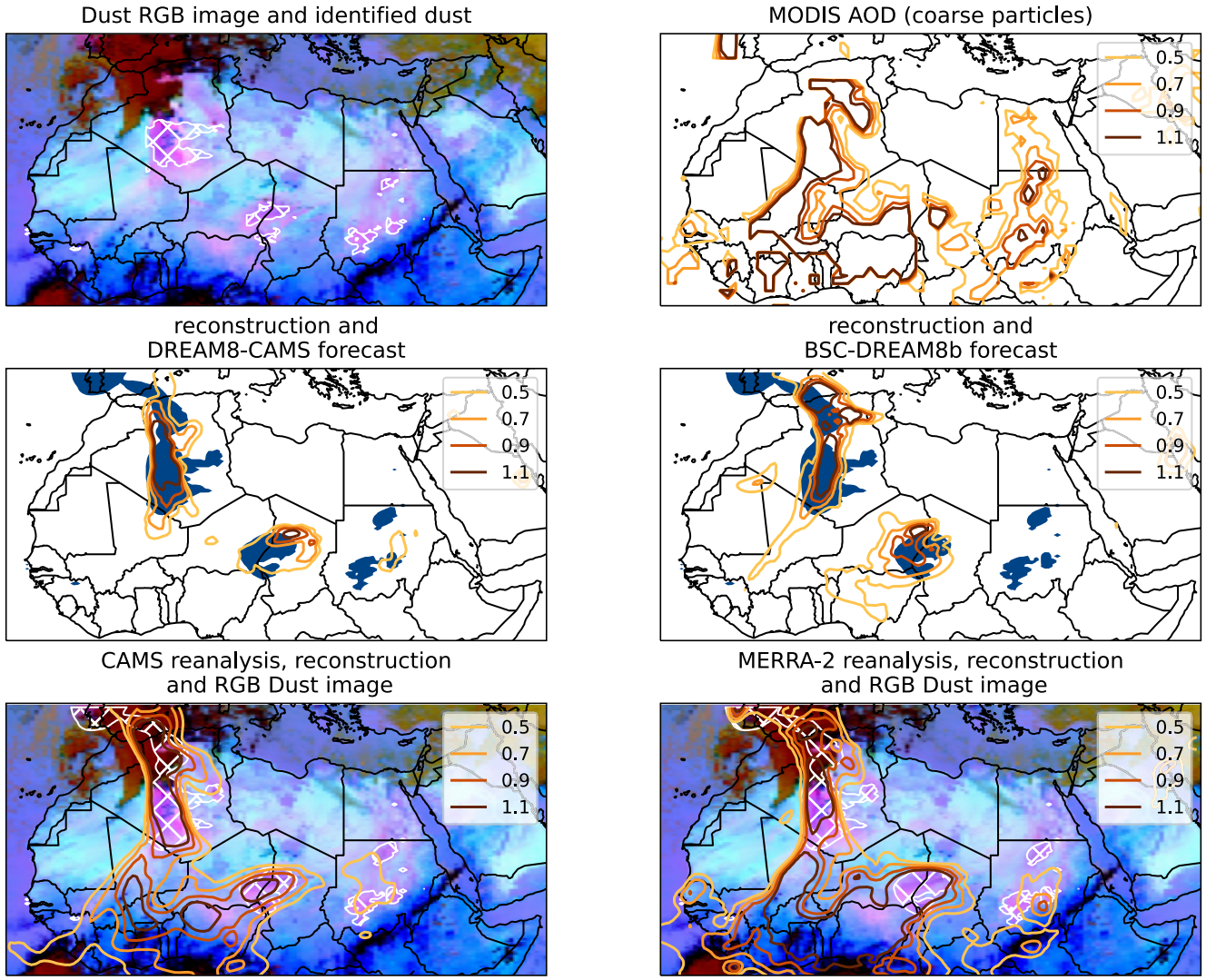

Figure 8. As Figure 7, but for 15 March 2022, 12 UTC. The top right panel shows observations from Moderate Resolution Imaging Spectroradiometer/Aqua. The middle right panel shows forecasts obtained from the BSC-DREAM8b model.

3.2. Comparing Reconstructions to Direct Observations

Calculating dust occurrence frequencies for each individual pixel provide an intuitive way of gauging the effect of the reconstructions. A comparison between reconstructed and directly observed, that is, non-reconstructed, annual dust occurrence frequency for 9 (left column), 12 (center column), and 15 (right column) UTC is shown in Figure 9. While a domain averaged dust occurrence frequency $\bar{f}_{\text{dust}}$, as indicated in the bottom right corner of the respective panels, does not reflect all the changes, it gives an indication, that a considerable amount of dust is commonly obscured by clouds. The red shading in the bottom panels indicates that compared to observations without reconstruction, the reconstructed images indicate an expected higher dust frequency. Differences of more than 2.5% points (pp, marked by a black isoline) are seen over the Atlantic Ocean and along the Atlantic coast. During all three times a considerable difference can be noted in the Tanezrouft Basin in the border region of Algeria and Mali. Furthermore, notable differences occur in the Bodélé Depression in Chad during all three time steps, however, their spatial extent is rather limited at 9 UTC. At 12 and 15 UTC differences can also be noted in Nubian Desert in Sudan and the Atlas Mountains and the Mediterranean coast in Algeria. The considerable differences at 15 UTC on the Arabian Peninsula should be taken with a grain of salt, since during parts of the year sun set on the Arabian Peninsula occurs earlier.

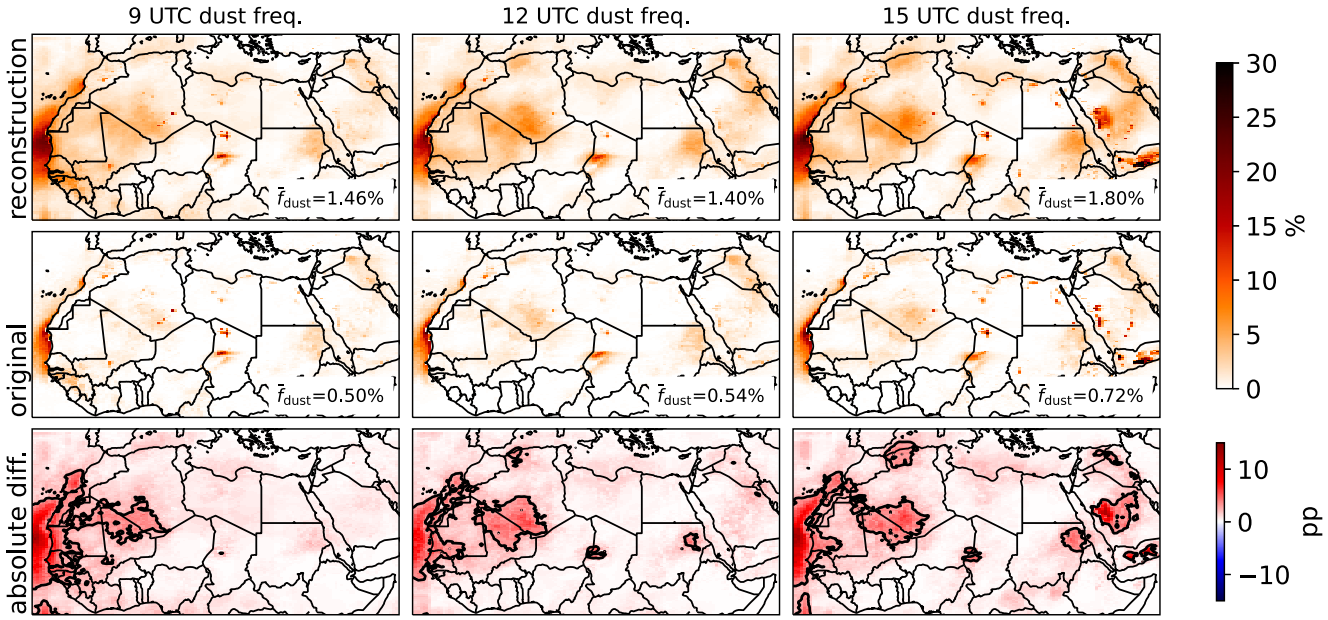

Figure 9. Dust occurrence frequencies at 9 (left column), 12 (center column), and 15 UTC (right column) derived from reconstructions (top row) and original observations (center row). The bottom row shows the absolute difference in dust occurrence frequency in percentage points (pp). The black isoline in the bottom row marks a difference of 2.5 pp.

Seasonal dust occurrence frequencies derived from reconstructed gray-scaled images and from direct observations (i.e., non-reconstructed gray-scale images) are shown for 9 and 12 UTC in Figure 10. Despite a coarser resolution compared to the full-resolution satellite images, the spatial patterns of seasonal dust occurrence from the reconstruction are remarkably consistent with the dust source activation frequency from March 2006 to February 2007 as reported by Schepanski et al. (2007). The spatial pattern for both 2021 and 2022 combined also shows consistency with the dust occurrence frequency derived from a combination of MODIS AOD data with Aerosol Index data from the Ozone Monitoring Instrument for 2005–2019 as reported by Gavrouzou et al. (2021). However, since we restored cloud-induced gaps and since we use a coarser resolution, we would expect a difference in magnitude and, thus, do not perform a quantitative comparison here. Since observations at 15 UTC may happen after sunset, as discussed above, the seasonal patterns for 15 UTC are not shown. With exception of summer (JJA), the reconstruction increases the dust occurrence frequency for both 9 and 12 UTC at the Bodélé Depression by more then 2.5. Particular high absolute differences over land can be noticed both 9 and 12 UTC during summer season in West Africa, reaching up to 15 pp at 12 UTC.

For daytime observations, higher values of τ_{dust} result on average in colors closer to magenta (Banks et al., 2019, specifically Figure 6 therein) and are therefore better represented in our reconstruction than weak dust events. This is consistent with our results, according to which a smaller value of ΔE_{cut} corresponds on average to higher values of τ_{dust} (Figure 11). Dust occurrence frequencies for $\Delta E_{cut} = 20$ corresponds to bright magenta, whereas the $\Delta E_{cut} = 51.9$ include more faded magenta shades and even faded purple shades (compare Figure 5). Our studies focuses on $\Delta E_{cut} = 51.9$, which captures most dust events and reduces the risk of misclassifications due to ambiguity of processes associated with colors that have a less pronounced pink component (see Section 2.2.2). For comparison the remaining panels of Figure 11 show the dust occurrence frequency obtained from CAMS reanalysis for dust events with $\tau_{dust} \geq 0.5$ (center left), $\tau_{dust} \geq 0.65$ (center right), $\tau_{dust} \geq 0.9$ (bottom left), and $\tau_{dust} \geq 1.1$ (bottom right). Visual inspection and calculation of the PSNR indicate that $\Delta E_{cut} = 20$ results in the closest match with $\tau_{dust} \geq 0.9$ and $\Delta E_{cut} = 51.9$ can be matched with $\tau_{dust} \geq 0.65$. Over ocean surfaces the perceptional color difference of $\Delta E_{cut} = 51.9$ corresponds to values of τ_{dust} of ~0.5, reflecting the influence of the surface conditions on the dust retrieval. Note, that based on the results by Banks et al. (2019) the number of dust events can be under-counted with a threshold of the perceptional color difference of $\Delta E_{cut} = 51.9$ (see Section 2.2.2). Our calculated dust occurrence frequency from the reconstructed dust images is therefore still a conservative estimate, even though dust underneath clouds is now accounted for.

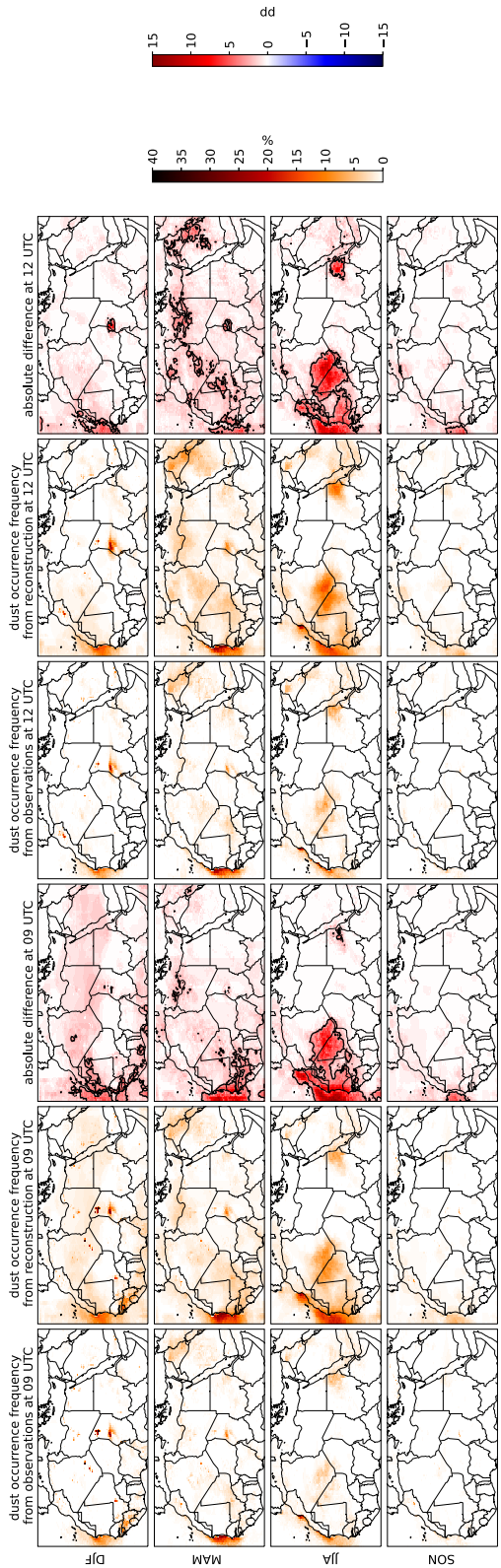

Figure 10.

The local maximum of the dust occurrence frequency from the reconstructed satellite images in the Nubian Desert (close to Sudan's Red Sea coast) is not represented by the CAMS reanalysis (see Figure 11). The Nubian Desert is a known dust source region as identified earlier in SEVIRI images (Schepanski et al., 2012), and also seen in other aerosol data, for example, the dust emission index derived from data of the Infrared Atmospheric Sounding Interferometer (Chédin et al., 2020) and the Aerosol Index using observations of the Total Ozone Mapping Spectrometer (N. J. Middleton & Goudie, 2001). Since the local maximum is also present in the dust frequency from non-reconstructed observations, the feature is not an artifact of the reconstruction. The feature is, however, present in dust occurrence frequencies derived from MERRA-2 reanalysis (see Figure S1 in Supporting Information S1). AOD data derived from MODIS sensors (MODIS Atmosphere Science Team, 2017a, 2017b) for coarse aerosol particles (Figure S2 in Supporting Information S1) indicates no optically thick, that is, $\tau \geq 0.7$, dust plumes in the Nubian Desert during both 2021 and 2022. However, MODIS aerosol data can be (partially) obscured by clouds.

This difference between CAMS reanalysis and reconstructions indicates, that the reanalysis cannot provide a ground truth for reconstructions. To further gauge the impact of the reconstruction, we calculated the SSIM and the PSNR for dust plumes obtained from reconstructions and the original observations with respect to a perfectly dust-free case at 9, 12, and 15 UTC simultaneously, shown in Figure 12. For both the SSIM and the PSNR the comparison between reconstruction and original observations indicate, that after the reconstruction the images become less similar to a perfectly dust-free case. In other words, the reconstruction increases the extents the extent of dust plumes. This is consistent with Figures 9 and 10.

3.3. Comparing the Reconstructions to Forecast Data

Here, we use the reconstructed images for a comparison with the output of dust forecast provided by the WMO Barcelona Dust Regional Center (see Section 2.1.2). Since qualitatively reconstructed images of areas with dust and quantitative forecasts of the dust AOD are not directly comparable, we first convert both the reconstructed gray-scale satellite images and the forecasted fields of τ_{dust} to binary images in which 1 represents a "dusty" pixel and 0 a dust-free pixel. In the case of the dust forecasts, a pixel is classified as dusty, if the AOD exceeds a pre-defined threshold, that is, $\tau \geq \tau_{threshold}$. For this purpose, we define and test six different thresholds: $\tau_{threshold} = [0.3, 0.5, 0.7, 0.9, 1.1, 1.3]$.

Figure 13 compares the dust forecast ensemble with respect to the median forecast, provided by the WMO Barcelona Dust Regional Center, and the forecast ensemble with respect to the reconstruction for both 2021 and 2022 combined. The columns represent the synoptic hours of 9 UTC (left column), 12 UTC (center column), and 15 UTC (right column). The evaluation metrics SSIM, directed Hausdorff distance, and PSNR (Section 2.2.4) are displayed as violin plots to evaluate the regional performance. As the median forecast is composed of the other model forecasts within the ensemble, we expect a larger number of cases with $SSIM \approx 1$ when we compare the individual forecast models against the median of all forecasts than for the reconstruction compared to the median of all forecasts. For small lower bounds of AOD ($\tau_{dust} \geq [0.3, 0.5]$) the distribution of SSIM values for forecasts compared to median forecasts strongly differ from the reconstructions compared to the median of forecasts. For intermediate AOD bounds ($\tau_{dust} = 0.7$) the difference

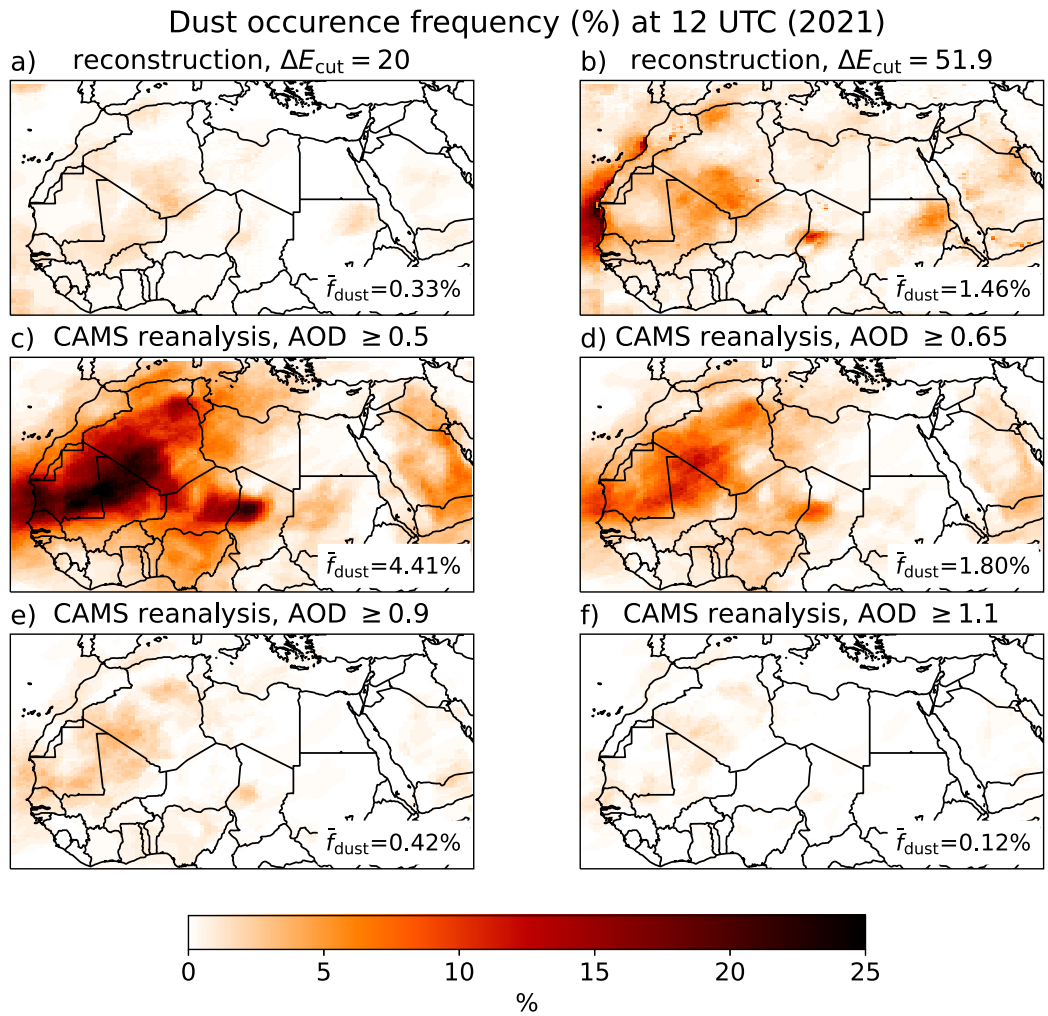

Figure 11. Comparison of dust occurrence frequency at 12 UTC in 2021 from reconstruction with different values of ΔE_{cut} (top row) and from Copernicus Atmosphere Monitoring Service reanalysis with different lower bounds of τ_{dust} (middle and bottom row). See Figure 5 for an interpretation aid of values of ΔE_{cut}.

in the value distributions is reduced, although for the reason outlined above the forecasts as a whole yield values of SSIM closer to 1. For larger values of AOD bounds $SSIM \rightarrow 1$, however, the forecasts converge faster to 1 than the reconstructions.

Using the directed Hausdorff distance as an evaluation criterion the reconstruction performs with respect to the dust forecast ensemble on average as well as the forecast ensemble compared to the median forecast for values of $\tau_{threshold} \geq 0.7$. In the case of PSNR, the reconstruction with respect to the forecast ensemble performs best for $\tau_{threshold} = 0.7$ compared to all model forecasts with respect to the median forecast, although the performance differences are not large. For $\tau_{threshold} \geq 0.9$ the median forecast outperforms the reconstruction with respect to the PSNR.

Figure 10. Seasonal dust frequency obtained from reconstructed gray-scaled images with $\Delta E_{cut} = 51.9$ at 9 UTC (first column, starting from the left) and from non-reconstructed gray-scaled images (second column). The third column shows the absolute difference between the first two columns. The fourth to sixth column are as the first to third column, but for 12 UTC. The rows represent the different seasons, from top to bottom winter (DJF), spring (MAM), summer (JJA), and autumn (SON). The black isoline in the third and sixth row marks an absolute difference of 2.5 pp. See Figure 5 for an interpretation aid of values of ΔE_{cut}. See Figure S3 in Supporting Information S1 for the corresponding overview with $\Delta E_{cut} = 20.0$.

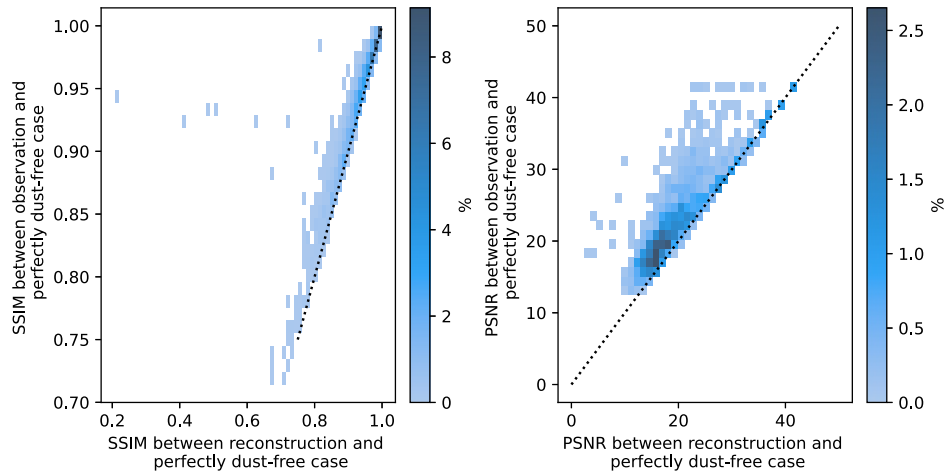

Figure 12. Two-dimensional histograms of the structural similarity index measure (left panel) and peak signal-to-noise ratio (right panel) of original observations and the reconstruction with respect to a perfectly dust-free case. Shading as in Figure 2. The dotted line indicates the 1:1 line.

Considering the SSIM as similarity measure, the reconstructions at 15 UTC are less similar with respect to the median forecast then the reconstructions at 9 and 12 UTC. While the value of $\Delta E_{\text{cut}} = 51.9$ was chosen for daytime observations and the parts of the SEVIRI image east of 25.5625°E may correspond to conditions after sunset, there is no discernible difference between the results shown in Figure 13 and the results obtained for the sub-set of the study area, which excludes longitude bands in which the sun set occurs before 15 UTC during any time of the year (shown in Figure S4 in Supporting Information S1).

We use the reconstruction of dust plumes to assess the level of similarity of dust-plume extents simulated by individual numerical forecasts over North Africa next. Figure 14 allows us to compare the reconstruction's performance against the output from individual forecast models at 12 UTC. In 2021 (top row) the models BSC-DREAM8b, DREAM8-CAMS, and WRF-NEMO agree best with the reconstruction as indicated by the respective median values of all three metrics. In 2022 (bottom row) the highest agreement in terms of PSNR and directed Hausdorff distance is seen for DREAM8-CAMS, MOCAGE, and WRF-NEMO, and in terms of SSIM for DREAM8-CAMS, MOCAGE, NCEP-GEFS, and ICON-ART. Only evaluating the spatial patterns, forecasts by LOTOS-EUROS and MONARCH show the least agreement with our reconstructions in both 2021 and 2022. While outperforming LOTOS-EUROS and MONARCH with respect to all three evaluation metrics, NCEP-GEFS showed the third lowest similarity to reconstructed SEVIRI dust plume observations in 2021. In 2022 NOA, which in 2021 narrowly outperformed NCEP-GEFS, had the third lowest similarity to the reconstructed plume observations. It should be noted, that among the best-performing models, both DREAM8-CAMS and MOCAGE use data assimilation of dust, while none of the models with comparatively poor performance used data assimilation techniques to incorporate dust information from observations. It should be stressed, that this brief evaluation has a focus on the spatial pattern of dust plumes as inferred from SEVIRI Dust RGB images, which was not done in the past. Typically, dust model forecasts are evaluated by their ability to correctly forecast τ at monitoring stations, most of which stem from sunphotometers that can only provide data during daytime in cloud-free conditions (cf. Huneeus et al., 2011; Terradellas et al., 2022). Hence, our study has demonstrated a new capability to evaluate simulated dust transport with a first consideration of dust plume shapes, based on computationally fast reconstructions of dust plumes in satellite images.

4. Discussion and Outlook

In this study, we restored spatial patterns of dust plumes from partially cloud-obscured satellite observations for the first time. Since both dust-aerosol emission and transport and cloud structures are governed by atmospheric conditions, we combined dust AOD data from CAMS reanalysis with coinciding SEVIRI-derived cloud-masks for the training of the ANN. The trained network was applied to cloud-masked, gray-scaled satellite images,

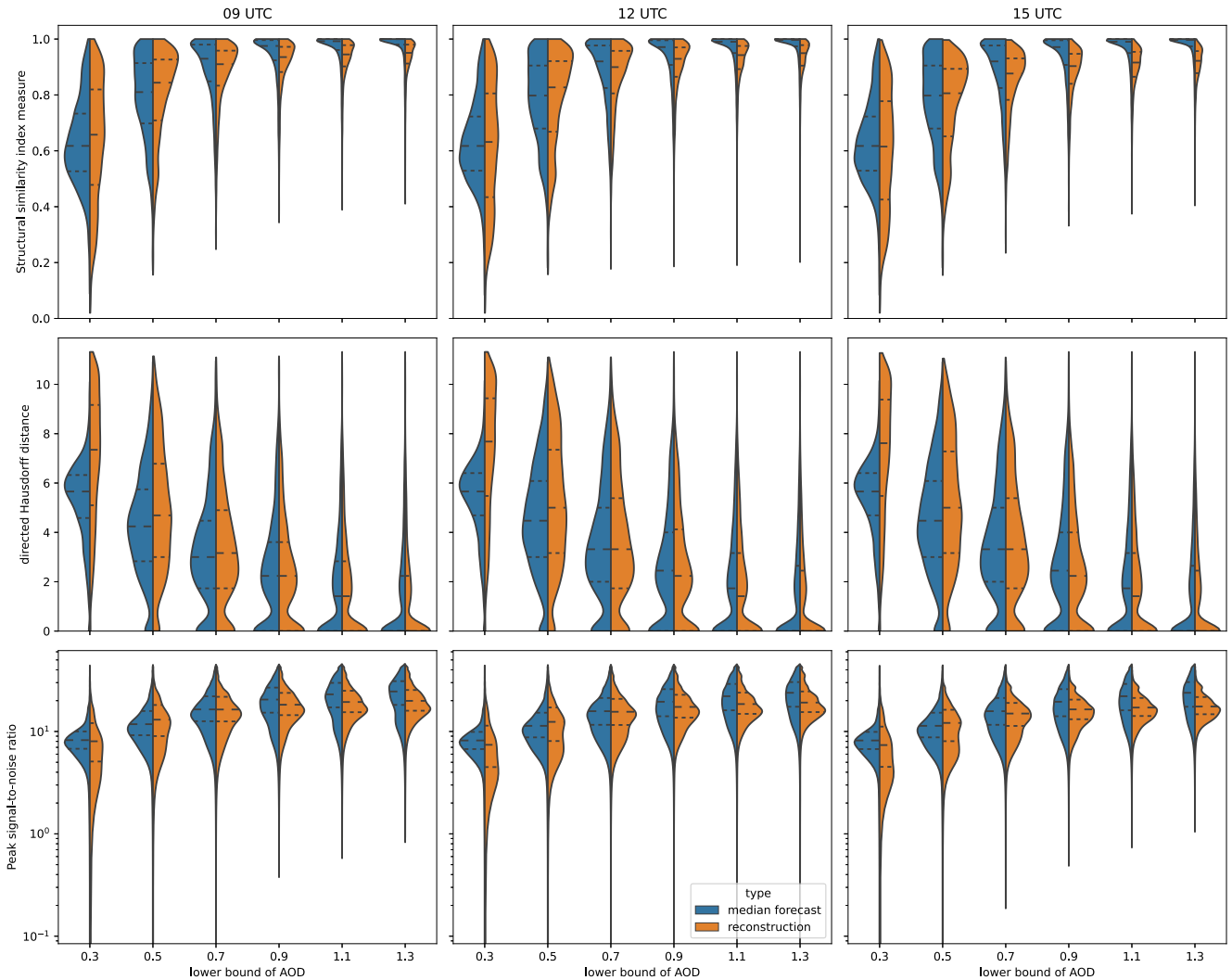

Figure 13. Comparison of the dust forecasts with respect to the median forecast (blue) and with respect to the reconstruction (orange) for 2021 and 2022 combined. Colors represent the respective quantity's distribution. Long dashed black lines represent the median and short dashed black lines the first and third quartile respectively. The columns represent the synoptic times of 09 UTC (left column), 12 UTC (center column), and 15 UTC (right column) The rows indicate different quality metrics, namely the structural similarity index measure (top row), directed Hausdorff distance (middle row), and peak signal-to-noise ratio (bottom row).

derived from MSG-SEVIRI's Dust RGB product. The reconstruction of dust plumes performs just as well or better than individual forecasts relative to the median across all forecasts.

So far parametrizations in numerical models provided a way of gauging the extent of below-cloud dust plumes, that is, of "seeing" beneath the clouds. By applying machine-learning-based in-painting methods to geostationary satellite images, we demonstrated another possibility of estimating the spatial patterns of dust plumes. Compared to numerical modeling, once the ANN is trained, our approach is computationally much cheaper than numerical modeling. Provided a SEVIRI Dust RGB image and the corresponding cloud mask are available, gray-scaling, data conversions, and subsequent in-painting for a single image required 30 s on a single core (AMD 7763 CPU, provided by DKRZ). Note, that this is an upper bound of required resources since the computational set-up was not streamlined for (near) real-time image processing.

Comparing the reconstructed and the directly observed dust occurrence frequencies during 2021 and 2022 for 9, 12, and 15 UTC (see Figure 9) indicates, that previous studies of the dust occurrence frequency and by extension the dust source activation frequency derived from SEVIRI and other satellite observations underestimate the dust occurrence and dust source activation due to the presence of clouds (e.g., Chédin et al., 2020; Heinold et al., 2013;

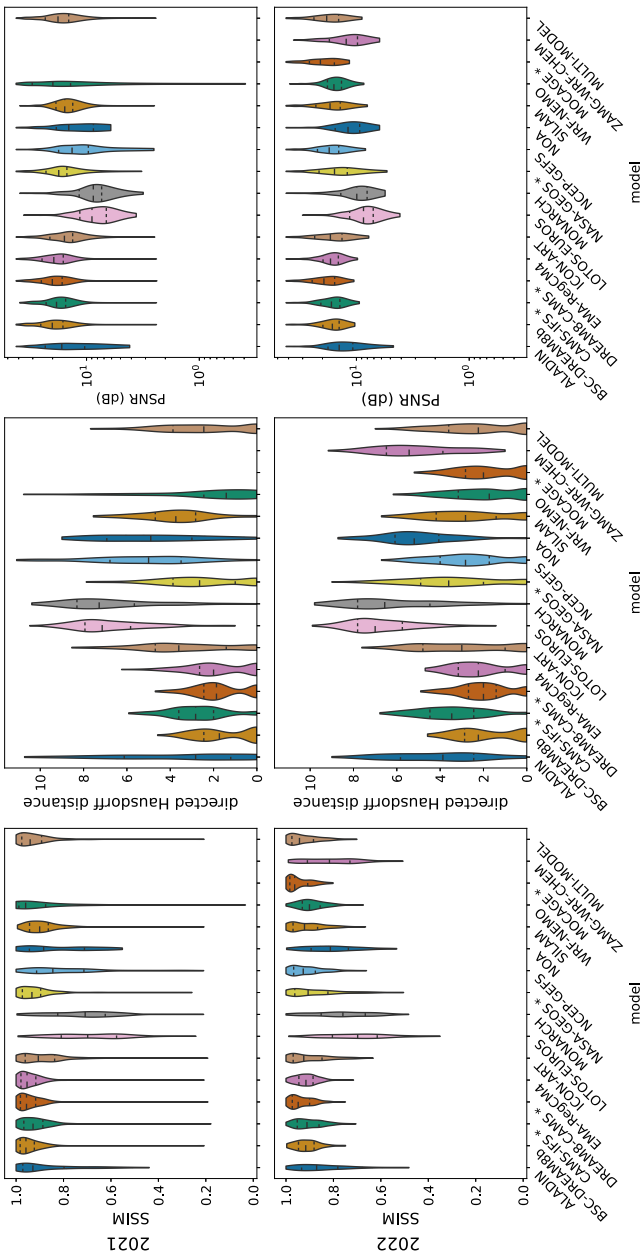

Figure 14. Comparison of the dust reconstruction with numerical forecasts with by the individual models in the ensemble provided by the World Meteorological Organization Barcelona Dust Regional Center for 2021 (top row) and 2022 (bottom row). The similarity measures shown are structural similarity index measure (left column), directed Hausdorff distance (center column), and peak signal-to-noise ratio (right column). As for Figure 13 the colors show the measures' distributions with long dashed black lines representing the median and short dashed black lines indicating the first and third quartile. Models marked with * use data assimilation. A full overview of the quartiles indicated by long-dashed (second quartile) and short-dashed (first and third quartile) lines is given in Tables S1 and S2 in Supporting Information S1.

Schepanski et al., 2012). Our results suggest that at least 0.78% of observations in the spatial mean over the entire region of interest miss dust plumes due to cloud coverage. Regionally and seasonally dust missed due to clouds can be up to 15% of observations. In extreme cases, all dust plumes occurring in an individual pixel are obscured by clouds. In 7.3% of pixels, all dust plumes as obtained by our proposed reconstruction method would be missed using conventional satellite observations. In 29.5% and 17.7% of pixels at least a tenth and a half of all dust plumes in the reconstruction, respectively, coincide with cloud coverage. When considering only the plumes with $\tau_{dust} \geq 0.65$ (see Figure 11) in the CAMS reanalysis as dust plumes, then for 9.6% of pixels of all dust plumes coincide with a cloud as observed by SEVIRI. A tenth and a half of dust plumes from CAMS reanalysis coincide with cloud coverage in 84.3% and 55.4% respectively of the pixels. Owning to our choice of identifying dust plumes by using gray-scaling based on perceptional color differences and due to the resolution of the input images, our number of dust plumes is still likely to be a conservative estimate, as indicated by the two case studies. In close proximity to clouds, the undercounting of dust-containing pixels can still be rectified by the ANN-based reconstruction method as illustrated in the first case study.

Since a similar Dust RGB composite is provided operationally for observations by the Advanced Baseline Imager instrument onboard the Geostationary Operational Environmental Satellite and the Advanced Himawari Imagers onboard the geostationary Himawari satellite, our approach could be transferred to other regions of interest (cf. Bessho et al., 2016; Fuell et al., 2016). While this study was focused on data from geostationary satellites the in-painting approach can also be adapted to observations and products from polar-orbiting satellites, such as AOD products derived from MODIS. Provided suitable training data from reanalysis is available the approach can further be applied to observations of different aerosol species and plumes of trace gases close to the respective source.

The here proposed method to restore dust plume extents on SEVIRI RGB Dust images by machine-learning-based image in-painting methods can be applied to a larger area and to images at a higher temporal resolution of up to 15 min in the case of SEVIRI. Such a spatial extension can facilitate additional investigations of dust transport to Europe and/or across the Atlantic Ocean. Using a higher temporal resolution may aid in studying dust transport mechanisms within North Africa in more detail and help to overcome observational gaps stemming from sparse ground-based observations.

There are a number of aspects in our current approach that can be further refined for future applications. To obtain a consistent spatio-temporal picture of suspended dust, including during nighttime, the values of ΔE_{cut} can be adjusted to the different environmental conditions, such as surface type (surface emissivity), skin temperature, and a climatology of column water vapor content (see Section 2.2.2 and Banks et al., 2019), for example, via generating look-up tables to account for these aspects. Adapting ΔE_{cut} to different environmental conditions would also be the next step to develop a link of the Dust RGB product or derived products, such as our reconstructed images, to τ_{dust}. Currently, there are already retrievals of dust AOD from SEVIRI observations based on look-up tables of observed shortwave reflectance (Brindley & Ignatov, 2006) for retrievals over ocean surfaces and based on longwave brightness temperatures in conjunction with European Center for Medium-Range Weather Forecasts' operational analysis for retrievals over land surfaces (Brindley & Russell, 2009), which could be exploited. Other retrieval algorithms involve optimal estimation (cf. Rodgers, 2000) based on observed brightness temperatures at both

visible and infrared channels (Carboni et al., 2007; Thomas et al., 2009). Following successfully established links between AOD and the color in the RGB Dust product, our method can restore the cloud-obscured fractions of AOD and subsequently contribute to assimilating further satellite observations into numerical models to better constrain the forecasts of dust. Accurate forecasts of dust plumes are important for different applications, for example, in the health and energy sector.

So far, each image has been reconstructed individually. With the help of recurrent neural networks (Che et al., 2018) the temporal evolution of dust storms can be taken into account explicitly by the network, thus, potentially further improving the reconstructions. While ground-based observations of dust in Northern Africa are sparse, incorporating these observations into the reconstructions provides another avenue for potential improvements in dust storm reconstruction for a better understanding of their evolution and accurate warnings of their impacts.

5. Conclusion

We present to our knowledge the first fast reconstruction of the spatial extent of partially cloud-obscured dust plumes from satellite observations. We achieve this by employing machine-learning-based image inpainting techniques. Once the ANN is trained, the reconstruction of dust plume extents is computationally inexpensive.

Spatially averaged over North Africa the differences in annual dust occurrence between reconstructions and classical satellite observations are small, not at last because dust is not present all the time across the entire of North Africa. However, the number of dust plumes obscured by clouds increases, when considering seasonal and regional subsets. As a conservative estimate, we find that up to 15% of satellite observations in West Africa and up to 10% of satellite observations in the Nubian Desert during 2021–2022 miss dust plumes. Based on the reconstructed plumes, in 7.3% of pixels, all dust plumes coincide with clouds and would, thus, not be directly identifiable from classical satellite observations. This roughly corresponds to a geographical area of $\sim 2 \cdot 10^6\,\mathrm{km}^2$. Our comparison with reanalysis indicates a somewhat higher fraction of 9.6% of pixels in which all dust plumes coincide with cloud cover.

The reconstructed dust plumes provide new means to validate and constrain spatial patterns of dust plumes in simulations from numerical forecast models and Earth system models. They further provide means for more detailed studies of dust emission and transport mechanisms using satellite observations free of gaps caused by cloud cover for the first time. The method can be applied to the corresponding dust products obtained from sensors on other geostationary satellites to compile a global data set. It can also be adapted to different types of aerosols and trace gases observed from geostationary and low-earth orbit satellites to broaden the possibilities for model validation of atmospheric composition in models, for example, as simulated by Earth system models in the Coupled Model Intercomparison Project or as used for operational air quality forecast models.

Conflict of Interest

The authors declare no conflicts of interest relevant to this study.

Data Availability Statement

The code for the ClimatereconstructionAI can be obtained from Zenodo (Inoue et al., 2022). The gray-scaling algorithm can be obtained from https://github.com/tobihose/Masterarbeit. Dust forecast datasets were provided by the WMO Barcelona Dust Regional Center and the partners of the Sand and Dust Storm Warning Advisory and Assessment System (SDS-WAS) for Northern Africa, the Middle East and Europe and can be obtained from https://dust.aemet.es. CAMS reanalysis data were provided by the Copernicus Atmospheric Monitoring Service (Inness et al., 2019a) and can be obtained from https://ads.atmosphere.copernicus.eu. SEVIRI false color RGB images (collection ID: EO:EUM:DAT:MSG:DUST, EUMETSAT, 2009b) and MSG cloud masks (collection ID: EO:EUM:DAT:MSG:CLM, EUMETSAT, 2009a) were provided by EUMETSAT and can be obtained from the EUMETSAT Data Store under https://data.eumetsat.int. MERRA-2 reanalysis data (Global Modeling and Assimilation Office & Pawson, 2015) was provided by the National Aeronautics and Space Administration's (NASA) Goddard Earth Science Data Information and Services Center (GES DISC) and can be obtained from

https://disc.gsfc.nasa.gov/datasets?project=MERRA-2. MODIS level 3 data (MODIS Atmosphere Science Team, 2017a, 2017b) was provided by NASA and can be obtained from https://ladsweb.modaps.eosdis.nasa.gov. Access to all datasets requires prior registration. In-painted images generated in the course of this study, as well as, trained ANNs are available via Zenodo (Kanngießer & Fiedler, 2024).

Acknowledgments
We acknowledge internal funding by the GEOMAR Helmholtz Centre for Ocean Research Kiel and University of Cologne for this work. We are grateful to Naoto Inoue, Christopher Kadow, and Stephan Seitz for making the climatereconstructionAI code publicly available and to Johannes Meuer and Étienne Plésiat for maintaining the code. Tobias Höschen is acknowledged for developing the gray-scaling algorithm as part of his master's thesis work, which was co-supervised by S. Fiedler. Dust forecast data was provided by the WMO Barcelona Dust Regional Center and the partners of the Sand and Dust Storm Warning Advisory and Assessment System (SDS-WAS) for Northern Africa, the Middle East and Europe. This work used resources of the Deutsches Klimarechenzentrum (DKRZ) granted by its Scientific Steering Committee (WLA) under project ID 1198. Open Access funding enabled and organized by Projekt DEAL.

References

Al-Hemoud, A., Al-Sudairawi, M., Neelamanai, S., Naseeb, A., & Behbehani, W. (2017). Socioeconomic effect of dust storms in Kuwait. *Arabian Journal of Geosciences*, *10*(1), 18. https://doi.org/10.1007/s12517-016-2816-9

Allen, C. J. T., & Washington, R. (2014). The low-level jet dust emission mechanism in the central Sahara: Observations from Bordj-Badji Mokhtar during the June 2011 Fennec intensive observation period. *Journal of Geophysical Research: Atmospheres*, *119*(6), 2990–3015. https://doi.org/10.1002/2013JD020594

Allen, C. J. T., Washington, R., & Engelstaedter, S. (2013). Dust emission and transport mechanisms in the central Sahara: Fennec ground-based observations from Bordj Badji Mokhtar, June 2011. *Journal of Geophysical Research: Atmospheres*, *118*(12), 6212–6232. https://doi.org/10.1002/jgrd.50534

Ashpole, I., & Washington, R. (2012). An automated dust detection using SEVIRI: A multiyear climatology of summertime dustiness in the central and western Sahara. *Journal of Geophysical Research*, *117*(D8), D08202. https://doi.org/10.1029/2011JD016845

Banks, J. R., Hünerbein, A., Heinold, B., Brindley, H. E., Deneke, H., & Schepanski, K. (2019). The sensitivity of the colour of dust in MSG-SEVIRI Desert Dust infrared composite imagery to surface and atmospheric conditions. *Atmospheric Chemistry and Physics*, *19*(10), 6893–6911. https://doi.org/10.5194/acp-19-6893-2019

Basart, S., Nickovic, S., Terradellas, E., Cuevas, E., Pérez García-Pando, C., García-Castrillo, G., et al. (2019). The WMO SDS-WAS regional center for northern Africa, Middle East and Europe. *E3S Web Conference*, *99*, 04008. https://doi.org/10.1051/e3sconf/20199904008

Basart, S., Pérez, C., Nickovic, S., Cuevas, E., & Baldasano, J. (2012). Development and evaluation of the BSC-DREAM8b dust regional model over Northern Africa, the Mediterranean and the Middle East. *Tellus B: Chemical and Physical Meteorology*, *64*(1), 18539. https://doi.org/10.3402/tellusb.v64i0.18539

Basart, S., Werner, E., Cuevas, E., & García-Pando, C. P. (2022). The WMO Barcelona dust regional center: Linking research with the development of dust user-oriented services. In C. Mensink & O. Jorba (Eds.), *Air pollution modeling and its application XXVIII* (pp. 223–229). Springer International Publishing.

Ben-Ami, Y., Koren, I., & Altaratz, O. (2009). Patterns of North African dust transport over the Atlantic: Winter vs. summer, based on CALIPSO first year data. *Atmospheric Chemistry and Physics*, *9*(20), 7867–7875. https://doi.org/10.5194/acp-9-7867-2009

Bessho, K., Date, K., Hayashi, M., Ikeda, A., Imai, T., Inoue, H., et al. (2016). An introduction to Himawari-8/9—Japan's new-generation geostationary meteorological satellites. *Journal of the Meteorological Society of Japanese Series II*, *94*(2), 151–183. https://doi.org/10.2151/jmsj.2016-009

Billet, E., Fedorov, A., & Chrisochoides, N. (2008). The use of robust local Hausdorff distances in accuracy assessment for image alignment of brain MRI. *The Insight Journal*. https://doi.org/10.54294/y57wd7

Bou Karam, D., Flamant, C., Cuesta, J., Pelon, J., & Williams, E. (2010). Dust emission and transport associated with a Saharan depression: February 2007 case. *Journal of Geophysical Research*, *115*(D4), 98. https://doi.org/10.1029/2009JD012390

Bou Karam, D., Williams, E., Janiga, M., Flamant, C., McGraw-Herdeg, M., Cuesta, J., et al. (2014). Synoptic-scale dust emissions over the Sahara Desert initiated by a moist convective cold pool in early August 2006. *Quarterly Journal of the Royal Meteorological Society*, *140*(685), 2591–2607. https://doi.org/10.1002/qj.2326

Brill, M. H. (1998). How the CIE 1931 color-matching functions were derived from Wright-Guild data. *Color Research & Application*, *23*(4), 259. https://doi.org/10.1002/(SICI)1520-6378(199808)23:4<259::AID-COL18>3.0.CO;2-7

Brindley, H., & Ignatov, A. (2006). Retrieval of mineral aerosol optical depth and size information from Meteosat Second Generation SEVIRI solar reflectance bands. *Remote Sensing of Environment*, *102*(3), 344–363. https://doi.org/10.1016/j.rse.2006.02.024

Brindley, H., & Russell, J. E. (2009). An assessment of Saharan dust loading and the corresponding cloud-free longwave direct radiative effect from geostationary satellite observations. *Journal of Geophysical Research*, *114*(D23), D21201. https://doi.org/10.1029/2008JD011635

Bristow, C. S., Hudson-Edwards, K. A., & Chappell, A. (2010). Fertilizing the amazon and equatorial Atlantic with west African dust. *Geophysical Research Letters*, *37*(14). https://doi.org/10.1029/2010GL043486

Brunet, D., Vrscay, E. R., & Wang, Z. (2012). On the mathematical properties of the structural similarity index. *IEEE Transactions on Image Processing*, *21*(4), 1488–1499. https://doi.org/10.1109/TIP.2011.2173206

Buseck, P. R., & Pósfai, M. (1999). Airborne minerals and related aerosol particles: Effects on climate and the environment. *Proceedings of the National Academy of Sciences of the United States of America*, *96*(7), 3372–3379. https://doi.org/10.1073/pnas.96.7.3372

Carboni, E., Thomas, G., Grainger, R., Poulsen, C., Siddans, R., Peters, D., et al. (2007). Retrieval of aerosol properties from SEVIRI using visible and infrared channels. In *Proceedings of EUMETSAT/AMS conference*.

Chauhan, R., Singh, A., & Saha, S. (2021). Cloud removal from satellite images. In *CoRR, abs/2112.15483*. Retrieved from https://arxiv.org/abs/2112.15483

Che, Z., Purushotham, S., Cho, K., Sontag, D., & Liu, Y. (2018). Recurrent neural networks for multivariate time series with missing values. *Scientific Reports*, *8*(1), 6085. https://doi.org/10.1038/s41598-018-24271-9

Chédin, A., Capelle, V., Scott, N. A., & Todd, M. C. (2020). Contribution of IASI to the observation of dust aerosol emissions (morning and nighttime) over the Sahara desert. *Journal of Geophysical Research: Atmospheres*, *125*(15), e2019JD032014. https://doi.org/10.1029/2019JD032014

Chen, Y., Tang, L., Yang, X., Fan, R., Bilal, M., & Li, Q. (2020). Thick clouds removal from multitemporal ZY-3 satellite images using deep learning. *IEEE Journal of Selected Topics in Applied Earth Observations and Remote Sensing*, *13*, 143–153. https://doi.org/10.1109/JSTARS.2019.2954130

Colarco, P., da Silva, A., Chin, M., & Diehl, T. (2010). Online simulations of global aerosol distributions in the NASA GEOS-4 model and comparisons to satellite and ground-based aerosol optical depth. *Journal of Geophysical Research*, *115*, D14. https://doi.org/10.1029/2009JD012820

Cui, Y., Ma, S., Yao, Z., Chen, X., Luo, Z., Fan, W., & Hong, Y. (2020). Developing a gap-filling algorithm using DNN for the Ts-VI triangle model to obtain temporally continuous daily actual evapotranspiration in an arid area of China. *Remote Sensing*, *12*(7), 1121. https://doi.org/10.3390/rs12071121

Czerkawski, M., Upadhyay, P., Davison, C., Werkmeister, A., Cardona, J., Atkinson, R., et al. (2022). Deep internal learning for inpainting of cloud-affected regions in satellite imagery. *Remote Sensing*, *14*(6), 1342. https://doi.org/10.3390/rs14061342

de la Beaujardiere, J. E. (2006). OpenGIS® Web Map server implementation specification. Version 1.3.0. Open Geospatial Consortium. (OGC;06-042). https://doi.org/10.25607/OBP-656

Dhital, S., Kaplan, M. L., Orza, J. A. G., & Fiedler, S. (2020). Atmospheric dynamics of a Saharan dust outbreak over Mindelo, Cape Verde Islands, preceded by Rossby wave breaking: Multiscale observational analyses and simulations. *Journal of Geophysical Research: Atmospheres*, *125*(18), e2020JD032975. https://doi.org/10.1029/2020JD032975

Di Mauro, B., Garzonio, R., Rossini, M., Filippa, G., Pogliotti, P., Galvagno, M., et al. (2019). Saharan dust events in the European Alps: Role in snowmelt and geochemical characterization. *The Cryosphere*, *13*(4), 1147–1165. https://doi.org/10.5194/tc-13-1147-2019

Dong, J., Yin, R., Sun, X., Li, Q., Yang, Y., & Qin, X. (2019). Inpainting of remote sensing SST images with deep convolutional generative adversarial network. *IEEE Geoscience and Remote Sensing Letters*, *16*(2), 173–177. https://doi.org/10.1109/LGRS.2018.2870880

El Amraoui, L., Plu, M., Guidard, V., Cornut, F., & Bacles, M. (2022). A pre-operational system based on the assimilation of MODIS aerosol optical depth in the MOCAGE chemical transport model. *Remote Sensing*, *14*(8), 1949. https://doi.org/10.3390/rs14081949

Elharrouss, O., Almaadeed, N., Al-Maadeed, S., & Akbari, Y. (2020). Image inpainting: A review. *Neural Processing Letters*, *51*(2), 2007–2028. https://doi.org/10.1007/s11063-019-10163-0

Enomoto, K., Sakurada, K., Wang, W., Fukui, H., Matsuoka, M., Nakamura, R., & Kawaguchi, N. (2017). Filmy cloud removal on satellite imagery with multispectral conditional generative adversarial nets. In *Proceedings of the IEEE conference on computer vision and pattern recognition (CVPR) workshops*.

EUMETSAT. (2009a). Cloud mask—MSG—0 degree [Dataset]. EUMETSAT. Retrieved from https://navigator.eumetsat.int/product/EO:EUM:DAT:MSG:CLM

EUMETSAT. (2009b). Dust RGB—MSG—0 degree [Dataset]. EUMETSAT. Retrieved from https://navigator.eumetsat.int/product/EO:EUM:DAT:MSG:DUST

Evan, A. T., Dunion, J., Foley, J. A., Heidinger, A. K., & Velden, C. S. (2006). New evidence for a relationship between Atlantic tropical cyclone activity and African dust outbreaks. *Geophysical Research Letters*, *33*(19), 297. https://doi.org/10.1029/2006GL026408

Evan, A. T., Flamant, C., Fiedler, S., & Doherty, O. (2014). An analysis of aeolian dust in climate models. *Geophysical Research Letters*, *41*(16), 5996–6001. https://doi.org/10.1002/2014GL060545

Fairman, H. S., Brill, M. H., & Hemmendinger, H. (1997). How the CIE 1931 color-matching functions were derived from Wright-Guild data. *Color Research & Application*, *22*(1), 11–23. https://doi.org/10.1002/(SICI)1520-6378(199702)22:1<11::AID-COL4>3.0.CO;2-7

Fiedler, S., Schepanski, K., Knippertz, P., Heinold, B., & Tegen, I. (2014). How important are atmospheric depressions and mobile cyclones for emitting mineral dust aerosol in North Africa? *Atmospheric Chemistry and Physics*, *14*(17), 8983–9000. https://doi.org/10.5194/acp-14-8983-2014

Flaounas, E., Kotroni, V., Lagouvardos, K., Klose, M., Flamant, C., & Giannaros, T. M. (2017). Sensitivity of the WRF-Chem (v3.6.1) model to different dust emission parametrisation: Assessment in the broader mediterranean region. *Geoscientific Model Development*, *10*(8), 2925–2945. https://doi.org/10.5194/gmd-10-2925-2017

Fromm, M., Kablick, G., III, & Caffrey, P. (2016). Dust-infused baroclinic cyclone storm clouds: The evidence, meteorology, and some implications. *Geophysical Research Letters*, *43*(24), 12643–12650. https://doi.org/10.1002/2016GL071801

Fuell, K., Guyer, B., Kann, D., Molthan, A., & Elmer, N. (2016). Next generation satellite RGB dust imagery leads to op-erational changes at NWS alburquerque. *Journal of Operational Meteorology*, *04*(06), 75–91. https://doi.org/10.15191/nwajom.2016.0406

Gabbi, J., Huss, M., Bauder, A., Cao, F., & Schwikowski, M. (2015). The impact of Saharan dust and black carbon on albedo and long-term mass balance of an alpine glacier. *The Cryosphere*, *9*(4), 1385–1400. https://doi.org/10.5194/tc-9-1385-2015

Gavrouzou, M., Hatzianastassiou, N., Gkikas, A., Korras-Carraca, M.-B., & Mihalopoulos, N. (2021). A global climatology of dust aerosols based on satellite data: Spatial, seasonal and inter-annual patterns over the period 2005–2019. *Remote Sensing*, *13*(3), 359. https://doi.org/10.3390/rs13030359

Gelaro, R., McCarty, W., Suárez, M. J., Todling, R., Molod, A., Takacs, L., et al. (2017). The Modern-Era Retrospective analysis for research and applications, version 2 (MERRA-2). *Journal of Climate*, *30*(14), 5419–5454. https://doi.org/10.1175/JCLI-D-16-0758.1

Global Modeling and Assimilation Office, & Pawson, S. (2015). MERRA-2 tavg1_2d_aer_nx: 2d, 1-hourly, time-averaged, single-level, assimilation, aerosol diagnostics v5.12.4 [Dataset]. NASA Goddard Earth Sciences Data and Information Services Center. https://doi.org/10.5067/KLICLTZ8EM9D

Goudie, A. S. (2009). Dust storms: Recent developments. *Journal of Environmental Management*, *90*(1), 89–94. https://doi.org/10.1016/j.jenvman.2008.07.007

Goudie, A. S. (2014). Desert dust and human health disorders. *Environment International*, *63*, 101–113. https://doi.org/10.1016/j.envint.2013.10.011

Griffin, D. W. (2007). Atmospheric movement of microorganisms in clouds of desert dust and implications for human health. *Clinical Microbiology Reviews*, *20*(3), 459–477. https://doi.org/10.1128/CMR.00039-06

Griffin, D. W., & Kellogg, C. A. (2004). Dust storms and their impact on ocean and human health: Dust in earth's atmosphere. *EcoHealth*, *1*(3), 284–295. https://doi.org/10.1007/s10393-004-0120-8

Heinold, B., Knippertz, P., Marsham, J. H., Fiedler, S., Dixon, N. S., Schepanski, K., et al. (2013). The role of deep convection and nocturnal low-level jets for dust emission in summertime West Africa: Estimates from convection-permitting simulations. *Journal of Geophysical Research: Atmospheres*, *118*(10), 4385–4400. https://doi.org/10.1002/jgrd.50402

Hintze, J. L., & Nelson, R. D. (1998). Violin plots: A box plot-density trace synergism. *The American Statistician*, *52*(2), 181–184. https://doi.org/10.1080/00031305.1998.10480559

Hoose, C., Kristjánsson, J. E., Chen, J.-P., & Hazra, A. (2010). A classical-theory-based parameterization of heterogeneous ice nucleation by mineral dust, soot, and biological particles in a global climate model. *Journal of the Atmospheric Sciences*, *67*(8), 2483–2503. https://doi.org/10.1175/2010JAS3425.1

Horé, A., & Ziou, D. (2013). Is there a relationship between peak-signal-to-noise ratio and structural similarity index measure? *IET Image Processing*, *7*(1), 12–24. https://doi.org/10.1049/iet-ipr.2012.0489

Hsu, N. C., Jeong, M.-J., Bettenhausen, C., Sayer, A. M., Hansell, R., Seftor, C. S., et al. (2013). Enhanced deep blue aerosol retrieval algorithm: The second generation. *Journal of Geophysical Research: Atmospheres*, *118*(16), 9296–9315. https://doi.org/10.1002/jgrd.50712

Huneeus, N., Basart, S., Fiedler, S., Morcrette, J.-J., Benedetti, A., Mulcahy, J., et al. (2016). Forecasting the northern African dust outbreak towards Europe in April 2011: A model intercomparison. *Atmospheric Chemistry and Physics*, *16*(8), 4967–4986. https://doi.org/10.5194/acp-16-4967-2016

Huneeus, N., Schulz, M., Balkanski, Y., Griesfeller, J., Prospero, J., Kinne, S., et al. (2011). Global dust model intercomparison in aerocom phase i. *Atmospheric Chemistry and Physics*, *11*(15), 7781–7816. https://doi.org/10.5194/acp-11-7781-2011

Huttenlocher, D., Klanderman, G., & Rucklidge, W. (1993). Comparing images using the Hausdorff distance. *IEEE Transactions on Pattern Analysis and Machine Intelligence*, *15*(9), 850–863. https://doi.org/10.1109/34.232073

Iizuka, S., Simo-Serra, E., & Ishikawa, H. (2017). Globally and locally consistent image completion. *ACM Transactions on Graphics*, *36*(4), 1–14. https://doi.org/10.1145/3072959.3073659

Inness, A., Ades, M., Agustí-Panareda, A., Barré, J., Benedictow, A., Blechschmidt, A.-M., et al. (2019a). CAMS global reanalysis (EAC4) [Dataset]. Copernicus Atmosphere Monitoring Service (CAMS) Atmosphere Data Store (ADS). Retrieved from https://ads.atmosphere.copernicus.eu/cdsapp#!/dataset/cams-global-reanalysis-eac4?tab=overview

Inness, A., Ades, M., Agustí-Panareda, A., Barré, J., Benedictow, A., Blechschmidt, A.-M., et al. (2019b). The CAMS reanalysis of atmospheric composition. *Atmospheric Chemistry and Physics*, *19*(6), 3515–3556. https://doi.org/10.5194/acp-19-3515-2019

Inoue, N., Seitz, S., Meuer, J., & Kadow, C. (2022). FREVA-CLINT/climatereconstructionAI: V1.0.2 [Software]. Zenodo. https://doi.org/10.5281/zenodo.6475858

International Electrotechnical Commission. (1999). Multimedia systems and equipment—Colour measurement and management—Part 2-1: Colour management—Default RGB colour space—sRGB (Standard No. IEC 61966-2-1:1999) [Software].

Jiao, L., Wu, H., Wang, H., & Bie, R. (2019). Multi-scale semantic image inpainting with residual learning and GAN. *Neurocomputing*, *331*, 199–212. https://doi.org/10.1016/j.neucom.2018.11.045

Jolliffe, I. T., & Stephenson, D. B. (2011). *Forecast verification a practitioner's guide in atmospheric science*. John Wiley & Sons.

Kadow, C., Hall, D. M., & Ulbrich, U. (2020). Artificial intelligence reconstructs missing climate information. *Nature Geoscience*, *13*(6), 408–413. https://doi.org/10.1038/s41561-020-0582-5

Kain, J. S., Weiss, S. J., Bright, D. R., Baldwin, M. E., Levit, J. J., Carbin, G. W., et al. (2008). Some practical considerations regarding horizontal resolution in the first generation of operational convection-allowing NWP. *Weather and Forecasting*, *23*(5), 931–952. https://doi.org/10.1175/WAF2007106.1

Kanngießer, F., & Fiedler, S. (2024). Machine-learning-based reconstruction of grey-scaled MSG-SEVIRI dust RGB images [Dataset]. Zenodo. https://doi.org/10.5281/ZENODO.8278518

Karanasiou, A., Moreno, N., Moreno, T., Viana, M., de Leeuw, F., & Querol, X. (2012). Health effects from Sahara dust episodes in Europe: Literature review and research gaps. *Environment International*, *47*, 107–114. https://doi.org/10.1016/j.envint.2012.06.012

King, M. D., Platnick, S., Menzel, W. P., Ackerman, S. A., & Hubanks, P. A. (2013). Spatial and temporal distribution of clouds observed by MODIS onboard the terra and aqua satellites. *IEEE Transactions on Geoscience and Remote Sensing*, *51*(7), 3826–3852. https://doi.org/10.1109/TGRS.2012.2227333

Klose, M., Jorba, O., Gonçalves Ageitos, M., Escribano, J., Dawson, M. L., Obiso, V., et al. (2021). Mineral dust cycle in the Multiscale Online Nonhydrostatic AtmospheRe CHemistry model (MONARCH) version 2.0. *Geoscientific Model Development*, *14*(10), 6403–6444. https://doi.org/10.5194/gmd-14-6403-2021

Knippertz, P., & Todd, M. C. (2012). Mineral dust aerosols over the Sahara: Meteorological controls on emission and transport and implications for modeling. *Reviews of Geophysics*, *50*(1), RG1007. https://doi.org/10.1029/2011RG000362

Kok, J. F., Adebiyi, A. A., Albani, S., Balkanski, Y., Checa-Garcia, R., Chin, M., et al. (2021). Contribution of the world's main dust source regions to the global cycle of desert dust. *Atmospheric Chemistry and Physics*, *21*(10), 8169–8193. https://doi.org/10.5194/acp-21-8169-2021

Kok, J. F., Storelvmo, T., Karydis, V. A., Adebiyi, A. A., Mahowald, N. M., Evan, A. T., et al. (2023). Mineral dust aerosol impacts on global climate and climate change. *Nature Reviews Earth & Environment*, *4*(2), 71–86. https://doi.org/10.1038/s43017-022-00379-5

Kontos, S., Kakosimos, K., Liora, N., Poupkou, A., & Melas, D. (2021). Towards a regional dust modeling system in the central middle east: Evaluation, uncertainties and recommendations. *Atmospheric Environment*, *246*, 118160. https://doi.org/10.1016/j.atmosenv.2020.118160

LeGrand, S. L., Polashenski, C., Letcher, T. W., Creighton, G. A., Peckham, S. E., & Cetola, J. D. (2019). The AFWA dust emission scheme for the GOCART aerosol model in WRF-Chem v3.8.1. *Geoscientific Model Development*, *12*(1), 131–166. https://doi.org/10.5194/gmd-12-131-2019

Lensky, I. M., & Rosenfeld, D. (2008). Clouds-aerosols-precipitation satellite analysis tool (CAPSAT). *Atmospheric Chemistry and Physics*, *8*(22), 6739–6753. https://doi.org/10.5194/acp-8-6739-2008

Li, J., Wu, Z., Hu, Z., Zhang, J., Li, M., Mo, L., & Molinier, M. (2020). Thin cloud removal in optical remote sensing images based on generative adversarial networks and physical model of cloud distortion. *ISPRS Journal of Photogrammetry and Remote Sensing*, *166*, 373–389. https://doi.org/10.1016/j.isprsjprs.2020.06.021

Liu, G., Reda, F. A., Shih, K. J., Wang, T.-C., Tao, A., & Catanzaro, B. (2018). Image inpainting for irregular holes using partial convolutions. In *Proceedings of the European conference on computer vision (ECCV)*.

Liu, L., & Hu, S. (2021). SACTNet: Spatial attention context transformation network for cloud removal. *Wireless Communications and Mobile Computing*, *2021*, 8292612–8292618. https://doi.org/10.1155/2021/8292612

Lu, C.-H., da Silva, A., Wang, J., Moorthi, S., Chin, M., Colarco, P., et al. (2016). The implementation of NEMS GFS Aerosol Component (NGAC) version 1.0 for global dust forecasting at NOAA/NCEP. *Geoscientific Model Development*, *9*(5), 1905–1919. https://doi.org/10.5194/gmd-9-1905-2016

Lutz, H.-J. (1999). Cloud processing for meteosat second generation. In *EUMETSAT Technical Department Technical Memorandum* (Vol. 4, p. 26).

Mahowald, N. M., Scanza, R., Brahney, J., Goodale, C. L., Hess, P. G., Moore, J. K., & Neff, J. (2017). Aerosol deposition impacts on land and ocean carbon cycles. *Current Climate Change Reports*, *3*(1), 16–31. https://doi.org/10.1007/s40641-017-0056-z

Malardel, S., Wedi, N., Deconinck, W., Diamantakis, M., Kuehnlein, C., Mozdzynski, G., et al. (2016). A new grid for the IFS. *ECMWF Newsletter*, *146*, 23–28. https://doi.org/10.21957/ZWDU9U5I

Manders, A. M. M., Builtjes, P. J. H., Curier, L., Denier van der Gon, H. A. C., Hendriks, C., Jonkers, S., et al. (2017). Curriculum vitae of the LOTOS–EUROS (v2.0) chemistry transport model. *Geoscientific Model Development*, *10*(11), 4145–4173. https://doi.org/10.5194/gmd-10-4145-2017

Middleton, N. (2017). Desert dust hazards: A global review. *Aeolian Research*, *24*, 53–63. https://doi.org/10.1016/j.aeolia.2016.12.001

Middleton, N. J., & Goudie, A. S. (2001). Saharan dust: Sources and trajectories. *Transactions of the Institute of British Geographers*, *26*(2), 165–181. https://doi.org/10.1111/1475-5661.00013

MODIS Atmosphere Science Team. (2017a). MODIS/terra aerosol cloud water vapor ozone daily L3 global 1deg CMG [Dataset]. NASA Level 1 and Atmosphere Archive and Distribution System. https://doi.org/10.5067/MODIS/MOD08_D3.061

MODIS Atmosphere Science Team. (2017b). Myd08_d3 MODIS/aqua aerosol cloud water vapor ozone daily l3 global 1deg CMG [Dataset]. NASA Level 1 and Atmosphere Archive and Distribution System. https://doi.org/10.5067/MODIS/MYD08_D3.061

Mokhtari, M., Gomes, L., Tulet, P., & Rezoug, T. (2012). Importance of the surface size distribution of erodible material: An improvement on the dust entrainment and deposition (DEAD) model. *Geoscientific Model Development*, *5*(3), 581–598. https://doi.org/10.5194/gmd-5-581-2012

Monteiro, A., Basart, S., Kazadzis, S., Votsis, A., Gkikas, A., Vandenbussche, S., et al. (2022). Multi-sectoral impact assessment of an extreme African dust episode in the Eastern Mediterranean in March 2018. *Science of the Total Environment*, *843*, 156861. https://doi.org/10.1016/j.scitotenv.2022.156861

Nickovic, S., Cvetkovic, B., Madonna, F., Rosoldi, M., Pejanovic, G., Petkovic, S., & Nikolic, J. (2016). Cloud ice caused by atmospheric mineral dust—Part 1: Parameterization of ice nuclei concentration in the NMME-DREAM model. *Atmospheric Chemistry and Physics*, *16*(17), 11367–11378. https://doi.org/10.5194/acp-16-11367-2016

Nickovic, S., Kallos, G., Papadopoulos, A., & Kakaliagou, O. (2001). A model for prediction of desert dust cycle in the atmosphere. *Journal of Geophysical Research*, *106*(D16), 18113–18129. https://doi.org/10.1029/2000JD900794

Oerlemans, J., Giesen, R., & Van Den Broeke, M. (2009). Retreating alpine glaciers: Increased melt rates due to accumulation of dust (Vadret da Morteratsch, Switzerland). *Journal of Glaciology*, *55*(192), 729–736. https://doi.org/10.3189/002214309789470969

Pajot, A., de Bézenac, E., & Gallinari, P. (2019). Unsupervised adversarial image in painting. In *CoRR, abs/1912.12164*. Retrieved from http://arxiv.org/abs/1912.12164

Palubinskas, G. (2014). Mystery behind similarity measures MSE and SSIM. In *2014 IEEE international conference on image processing (ICIP)* (pp. 575–579). https://doi.org/10.1109/ICIP.2014.7025115

Pan, H. (2020). Cloud removal for remote sensing imagery via spatial attention generative adversarial network. *arXiv*. https://doi.org/10.48550/ARXIV.2009.13015

Pejanovic, G., Vukovic, A., Vujadinovic, M., & Dacic, M. (2010). Assimilation of satellite information on mineral dust using dynamic relaxation approach. In *EGU general assembly conference abstracts* (p. 7353)

Pérez, C., Haustein, K., Janjic, Z., Jorba, O., Huneeus, N., Baldasano, J. M., et al. (2011). Atmospheric dust modeling from meso to global scales with the online NMMB/BSC-dust model—Part 1: Model description, annual simulations and evaluation. *Atmospheric Chemistry and Physics*, *11*(24), 13001–13027. https://doi.org/10.5194/acp-11-13001-2011

Pérez, C., Nickovic, S., Pejanovic, G., Baldasano, J. M., & Özsoy, E. (2006). Interactive dust-radiation modeling: A step to improve weather forecasts. *Journal of Geophysical Research*, *111*(D16), D16206. https://doi.org/10.1029/2005JD006717

Pósfai, M., & Buseck, P. R. (2010). Nature and climate effects of individual tropospheric aerosol particles. *Annual Review of Earth and Planetary Sciences*, *38*(1), 17–43. https://doi.org/10.1146/annurev.earth.031208.100032

Qin, Z., Zeng, Q., Zong, Y., & Xu, F. (2021). Image inpainting based on deep learning: A review. *Displays*, *69*, 102028. https://doi.org/10.1016/j.displa.2021.102028

Randles, C. A., da Silva, A. M., Buchard, V., Colarco, P. R., Darmenov, A., Govindaraju, R., et al. (2017). The MERRA-2 aerosol reanalysis, 1980 onward. Part I: System description and data assimilation evaluation. *Journal of Climate*, *30*(17), 6823–6850. https://doi.org/10.1175/JCLI-D-16-0609.1

Randles, C. A., da Silva, A. M., Buchard, V., Darmenov, A., Colarco, P. R., Aquila, V., et al. (2016). The MERRA-2 aerosol assimilation (technical report no. NASA/TM-2016-104606). In *Technical report series on global modeling and data assimilation* (Vol. 45). National Aeronautics and Space Administration, Goddard Space Flight Center. Retrieved from https://gmao.gsfc.nasa.gov/pubs/docs/Randles887.pdf

Rémy, S., Kipling, Z., Flemming, J., Boucher, O., Nabat, P., Michou, M., et al. (2019). Description and evaluation of the tropospheric aerosol scheme in the European Centre for medium-range weather forecasts (ECMWF) integrated forecasting system (IFS-AER, cycle 45r1). *Geoscientific Model Development*, *12*(11), 4627–4659. https://doi.org/10.5194/gmd-12-4627-2019

Rieger, D., Bangert, M., Bischoff-Gauss, I., Förstner, J., Lundgren, K., Reinert, D., et al. (2015). ICON-ART 1.0—A new online-coupled model system from the global to regional scale. *Geoscientific Model Development*, *8*(6), 1659–1676. https://doi.org/10.5194/gmd-8-1659-2015

Roberts, A. J., & Knippertz, P. (2014). The formation of a large summertime Saharan dust plume: Convective and synoptic-scale analysis. *Journal of Geophysical Research: Atmospheres*, *119*(4), 1766–1785. https://doi.org/10.1002/2013JD020667

Robertson, A. R. (1990). Historical development of CIE recommended color difference equations. *Color Research & Application*, *15*(3), 167–170. https://doi.org/10.1002/col.5080150308

Rodgers, C. D. (2000). *Inverse methods for atmospheric sounding: Theory and practice*. World Scientific.

Ronneberger, O., Fischer, P., & Brox, T. (2015). U-Net: Convolutional networks for biomedical image segmentation. *arXiv*. https://doi.org/10.48550/ARXIV.1505.04597

Sarafanov, M., Kazakov, E., Nikitin, N. O., & Kalyuzhnaya, A. V. (2020). A machine learning approach for remote sensing data gap-filling with open-source implementation: An example regarding land surface temperature, surface albedo and NDVI. *Remote Sensing*, *12*(23), 3865. https://doi.org/10.3390/rs12233865

Sarukkai, V., Jain, A., Uzkent, B., & Ermon, S. (2020). Cloud removal from satellite images using spatiotemporal generator networks. In *Proceedings of the IEEE/CVF winter conference on applications of computer vision (WACV)*.

Sayer, A. M., Hsu, N. C., Bettenhausen, C., & Jeong, M.-J. (2013). Validation and uncertainty estimates for modis collection 6 "deep blue" aerosol data. *Journal of Geophysical Research: Atmospheres*, *118*(14), 7864–7872. https://doi.org/10.1002/jgrd.50600

Schanda, J. (Ed.) (2007). *Colorimetry*. Wiley.

Schepanski, K., & Knippertz, P. (2011). Soudano-Saharan depressions and their importance for precipitation and dust: A new perspective on a classical synoptic concept. *Quarterly Journal of the Royal Meteorological Society*, *137*(659), 1431–1445. https://doi.org/10.1002/qj.850

Schepanski, K., Tegen, I., Laurent, B., Heinold, B., & Macke, A. (2007). A new Saharan dust source activation frequency map derived from MSG-SEVIRI IR-channels. *Geophysical Research Letters*, *34*(18), L18803. https://doi.org/10.1029/2007GL030168

Schepanski, K., Tegen, I., & Macke, A. (2012). Comparison of satellite based observations of Saharan dust source areas. *Remote Sensing of Environment*, *123*, 90–97. https://doi.org/10.1016/j.rse.2012.03.019

Schmetz, J., Pili, P., Tjemkes, S., Just, D., Kerkmann, J., Rota, S., & Ratier, A. (2002). An introduction to meteosat second generation (MSG). *Bulletin of the American Meteorological Society*, *83*(7), 977–992. https://doi.org/10.1175/1520-0477(2002)083<0977:AITMSG>2.3.CO;2

Schulzweida, U. (2021). CDO user guide. *Zenodo*. https://doi.org/10.5281/zenodo.5614769

Seifert, A., Bachmann, V., Filipitsch, F., Förstner, J., Grams, C. M., Hoshyaripour, G. A., et al. (2023). Aerosol–cloud–radiation interaction during Saharan dust episodes: The dusty cirrus puzzle. *Atmospheric Chemistry and Physics*, *23*(11), 6409–6430. https://doi.org/10.5194/acp-23-6409-2023

Seifert, P., Ansmann, A., Mattis, I., Wandinger, U., Tesche, M., Engelmann, R., et al. (2010). Saharan dust and heterogeneous ice formation: Eleven years of cloud observations at a central European EARLINET site. *Journal of Geophysical Research*, *115*(D20), D20201. https://doi.org/10.1029/2009JD013222

Singh, P., & Komodakis, N. (2018). Cloud-gan: Cloud removal for Sentinel-2 imagery using a cyclic consistent generative adversarial networks. In *IGARSS 2018—2018 IEEE international Geoscience and remote sensing symposium* (pp. 1772–1775). https://doi.org/10.1109/IGARSS.2018.8519033

Sofiev, M., Vira, J., Kouznetsov, R., Prank, M., Soares, J., & Genikhovich, E. (2015). Construction of the SILAM Eulerian atmospheric dispersion model based on the advection algorithm of Michael Galperin. *Geoscientific Model Development*, *8*(11), 3497–3522. https://doi.org/10.5194/gmd-8-3497-2015

Solomos, S., Ansmann, A., Mamouri, R.-E., Binietoglou, I., Patlakas, P., Marinou, E., & Amiridis, V. (2017). Remote sensing and modelling analysis of the extreme dust storm hitting the middle east and eastern mediterranean in September 2015. *Atmospheric Chemistry and Physics*, *17*(6), 4063–4079. https://doi.org/10.5194/acp-17-4063-2017

Stefanski, R., & Sivakumar, M. V. K. (2009). Impacts of sand and dust storms on agriculture and potential agricultural applications of a SDSWS. *IOP Conference Series: Earth and Environmental Science*, *7*(1), 012016. https://doi.org/10.1088/1755-1307/7/1/012016

Stock, A., Subramaniam, A., Van Dijken, G. L., Wedding, L. M., Arrigo, K. R., Mills, M. M., et al. (2020). Comparison of cloud-filling algorithms for marine satellite data. *Remote Sensing*, *12*(20), 3313. https://doi.org/10.3390/rs12203313

Strong, J. D. O., Vecchi, G. A., & Ginoux, P. (2018). The climatological effect of Saharan dust on global tropical cyclones in a fully coupled GCM. *Journal of Geophysical Research: Atmospheres*, *123*(10), 5538–5559. https://doi.org/10.1029/2017JD027808

Swap, R., Garstang, M., Greco, S., Talbot, R., & Kållberg, P. (1992). Saharan dust in the amazon basin. *Tellus B: Chemical and Physical Meteorology*, *44*(2), 133–149. https://doi.org/10.1034/j.1600-0889.1992.t01-1-00005.x

Taha, A. A., & Hanbury, A. (2015). An efficient algorithm for calculating the exact Hausdorff distance. *IEEE Transactions on Pattern Analysis and Machine Intelligence*, *37*(11), 2153–2163. https://doi.org/10.1109/TPAMI.2015.2408351

Talbot, R. W., Harriss, R. C., Browell, E. V., Gregory, G. L., Sebacher, D. I., & Beck, S. M. (1986). Distribution and geochemistry of aerosols in the tropical North Atlantic troposphere: Relationship to Saharan dust. *Journal of Geophysical Research*, *91*(D4), 5173–5182. https://doi.org/10.1029/JD091iD04p05173

Tanaka, T. Y., & Chiba, M. (2006). A numerical study of the contributions of dust source regions to the global dust budget. *Global and Planetary Change*, *52*(1), 88–104. https://doi.org/10.1016/j.gloplacha.2006.02.002

Termonia, P., Fischer, C., Bazile, E., Bouyssel, F., Brožková, R., Bénard, P., et al. (2018). The ALADIN system and its canonical model configurations AROME CY41T1 and ALARO CY40T1. *Geoscientific Model Development*, *11*(1), 257–281. https://doi.org/10.5194/gmd-11-257-2018

Terradellas, E., Basart, S., Werner, E., & Benincas, F. (2022). *Model inter-comparison and evaluation of dust forecasts (technical report no. SDS-WAS-2020-001)*. Sand and Dust Storm Warning Advisory and Assessment System (SDS-WAS) Regional Center for Northern Africa-Middle East-Europe (NAMEE).

Thomas, G. E., Carboni, E., Sayer, A. M., Poulsen, C. A., Siddans, R., & Grainger, R. G. (2009). Oxford-RAL aerosol and cloud (ORAC): Aerosol retrievals from satellite radiometers. In A. A. Kokhanovsky & G. de Leeuw (Eds.), *Satellite aerosol remote sensing over land* (pp. 193–225). Springer. https://doi.org/10.1007/978-3-540-69397-0_7

Trzeciak, T. M., Garcia-Carreras, L., & Marsham, J. H. (2017). Cross-Saharan transport of water vapor via recycled cold pool outflows from moist convection. *Geophysical Research Letters*, *44*(3), 1554–1563. https://doi.org/10.1002/2016GL072108

van der Walt, S., Schönberger, J. L., Nunez-Iglesias, J., Boulogne, F., Warner, J. D., Yager, N., et al. (2014). scikit-image: Image processing in python. *PeerJ*, *2*, e453. https://doi.org/10.7717/peerj.453

Virtanen, P., Gommers, R., Oliphant, T. E., Haberland, M., Reddy, T., Cournapeau, D., et al. (2020). SciPy 1.0: Fundamental algorithms for scientific computing in Python. *Nature Methods*, *17*(3), 261–272. https://doi.org/10.1038/s41592-019-0686-2

Wang, Q., Gu, J., & Wang, X. (2020). The impact of Sahara dust on air quality and public health in European countries. *Atmospheric Environment*, *241*, 117771. https://doi.org/10.1016/j.atmosenv.2020.117771

Wang, Z., Bovik, A., Sheikh, H., & Simoncelli, E. (2004). Image quality assessment: From error visibility to structural similarity. *IEEE Transactions on Image Processing*, *13*(4), 600–612. https://doi.org/10.1109/TIP.2003.819861

Weisman, M. L., Skamarock, W. C., & Klemp, J. B. (1997). The resolution dependence of explicitly modeled convective systems. *Monthly Weather Review*, *125*(4), 527–548. https://doi.org/10.1175/1520-0493(1997)125<0527:TRDOEM>2.0.CO;2

Weiss, D. J., Atkinson, P. M., Bhatt, S., Mappin, B., Hay, S. I., & Gething, P. W. (2014). An effective approach for gap-filling continental scale remotely sensed time-series. *ISPRS Journal of Photogrammetry and Remote Sensing*, *98*, 106–118. https://doi.org/10.1016/j.isprsjprs.2014.10.001

Yu, H., Tan, Q., Zhou, L., Zhou, Y., Bian, H., Chin, M., et al. (2021). Observation and modeling of the historic "Godzilla" African dust intrusion into the Caribbean basin and the southern us in June 2020. *Atmospheric Chemistry and Physics*, *21*(16), 12359–12383. https://doi.org/10.5194/acp-21-12359-2021

Yu, J., Lin, Z., Yang, J., Shen, X., Lu, X., & Huang, T. S. (2018). Generative image inpainting with contextual attention. In *Proceedings of the IEEE conference on computer vision and pattern recognition (CVPR)*.

Zakey, A. S., Solmon, F., & Giorgi, F. (2006). Implementation and testing of a desert dust module in a regional climate model. *Atmospheric Chemistry and Physics*, *6*(12), 4687–4704. https://doi.org/10.5194/acp-6-4687-2006

Zhao, A., Ryder, C. L., & Wilcox, L. J. (2022). How well do the CMIP6 models simulate dust aerosols? *Atmospheric Chemistry and Physics*, *22*(3), 2095–2119. https://doi.org/10.5194/acp-22-2095-2022

Zhao, M., Olsen, P. A., & Chandra, R. (2021). Seeing through clouds in satellite images. In *CoRR, abs/2106.08408*. Retrieved from https://arxiv.org/abs/2106.08408

Zhao, W., & Duan, S.-B. (2020). Reconstruction of daytime land surface temperatures under cloud-covered conditions using integrated MODIS/Terra land products and MSG geostationary satellite data. *Remote Sensing of Environment*, *247*, 111931. https://doi.org/10.1016/j.rse.2020.111931

Zi, Y., Xie, F., Song, X., Jiang, Z., & Zhang, H. (2022). Thin cloud removal for remote sensing images using a physical-model-based CycleGAN with unpaired data. *IEEE Geoscience and Remote Sensing Letters*, *19*, 1–5. https://doi.org/10.1109/LGRS.2021.3140033